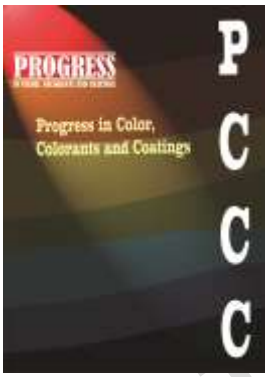
ACCEPTED MANUSCRIPT

Accepted Manuscript



Title: Phase composition of $Ca_4Al_6CrO_{16}$-based pigments for high-performance polymer coloration: Experimental study supported by DFT+U calculations

Authors: M. Jalili, M. Khajeh Aminian, L Gholamzadeh, S.Y. Vaselnia

Manuscript number**: PCCC-2609-1540**

To appear in: Progresss in Color, Colorants and Coatings

Received: 5 September 2026

Final Revised: 6 November 2026

Accepted: 8 November 2026

Please cite this article as:

M. Jalili, M. Khajeh Aminian, L Gholamzadeh, S.Y. Vaselnia, Phase composition of $Ca_4Al_6CrO_{16}$-based pigments for high-performance polymer coloration: Experimental study supported by DFT+U calculations, Prog. Color, Colorants, Coat., 20 (2027) XX-XXX.

DOI: 10.30509/pccc.2026.167876.1540

This is a PDF file of the unedited manuscript that has been accepted for publication. The manuscript will undergo copyediting, typesetting, and review of the resulting proof before it is published in its final form

ACCEPTED MANUSCRIPT

Phase Composition of $Ca_4Al_6CrO_{16}$-based Pigments for High-performance Polymer Coloration: Experimental Study Supported by DFT+U Calculations

M. Jalili[1], M. Khajeh Aminian[1]*, L Gholamzadeh[2], S.Y. Vaselnia [1]

[1] Nano Pigments and Coatings Laboratory, Department of Physics, Yazd University, P.O. Box: 89195-741, Yazd, Iran

[2] Department of Physics, Yazd University, P.O. Box: 89195-741, Yazd, Iran

E-mail address: kh.aminian@yazd.ac.ir

Accepted Manuscript

Abstract

A $Ca_4Al_6CrO_{16}$-based chromium-containing calcium aluminate pigment was investigated through an integrated experimental–computational study, with emphasis on its suitability for polyurethane coloration. The synthesized powders were characterized by X-ray diffraction (XRD), scanning electron microscopy (SEM), UV-Visible diffuse-reflectance spectroscopy, and CIELAB colorimetry to establish relationships among phase composition, morphology, and chromatic response. The experimental results confirmed the formation of the cubic $Ca_4Al_6CrO_{16}$ phase, with LY_1 exhibiting a single-phase composition. Among the pigments synthesized at 1200 °C, LY_4 showed the smallest average particle size (630 nm) and the highest b* value (67.4), along with the lowest a* value, indicating the highest yellow purity among the synthesized pigments. The corresponding polyurethane coating also exhibited the highest yellowness, with a b* value of 75.9. To elucidate the intrinsic electronic characteristics of the pigment, first-principles calculations were performed within the DFT+U framework, considering the localized Cr 3d states. The calculated band structure, DOS, PDOS, charge-density

ACCEPTED MANUSCRIPT

distribution, and electron localization function (ELF) were used to examine the electronic and bonding characteristics of $Ca_4Al_6CrO_{16}$. The calculations revealed pronounced contributions from Cr 3d and O 2p states and significant Cr–O orbital interactions. The calculated cohesive energy of -5.64 eV atom^{-1} and total magnetization of 8.00 μB/cell further characterize the structural and magnetic properties of the phase. Overall, the combined experimental and computational results demonstrate the structural stability, characteristic yellow coloration, and promising applicability of $Ca_4Al_6CrO_{16}$-based pigments in polyurethane coloration systems.

Keywords: $Ca_4Al_6CrO_{16}$; Polymer Coloration; DFT+U; Optical Properties; Color Performance.

1. Introduction

Polyurethane (PU) is one of the most widely used polymer matrices for high-performance coatings due to its excellent mechanical properties, chemical resistance, and versatility in formulation. PU coatings are extensively employed in automotive, industrial, and protective applications where durability and color stability are critical requirements [1-3]. The integration of inorganic pigments into PU matrices enables the development of colored coatings that combine the thermal robustness and chemical durability of ceramic pigments with the flexibility and processability of organic polymers [2, 4].

The dispersion quality and particle size of pigments within the polymer matrix are decisive factors affecting the optical performance and mechanical integrity of the final

ACCEPTED MANUSCRIPT

coating. Submicron- and nano-scale pigment particles (<1 μm) offer enhanced color strength and improved light scattering characteristics due to their higher specific surface area. However, the high surface energy of fine particles inevitably leads to agglomeration, which negatively impacts both the chromatic properties and the surface smoothness of PU coatings. Therefore, achieving uniform dispersion and controlling particle size distribution are essential prerequisites for developing high-performance polymer-grade inorganic pigments [1, 3, 5].

Outside traditional ceramic uses, inorganic pigments are increasingly employed in automotive finishes, polymeric media, and heat-reflective roofing systems because of their mechanical robustness, resistance to corrosion, and chemical durability [6-10]. In this context, the integration of structurally stable oxide pigments into polymer matrices has attracted growing attention as a strategy for achieving durable coloration without compromising mechanical or thermal performance.

Inorganic pigments are employed extensively in inks, paints, glazes, surface coatings, and functional composite systems because they can retain their properties under severe thermal and chemical conditions [8, 11-15]. Their performance is strongly influenced by characteristics such as particle-size distribution, morphology, optical response, and chemical composition [16-18].

Within the family of chromium-based pigments, $Ca_4Al_6CrO_{16}$ has emerged as a relatively unexplored material with considerable potential for yellow pigmentation [19, 20]. The presence of Cr(VI) ions within the aluminate lattice results in a distinctive yellow hue while preserving structural stability up to approximately 1500 °C [21-23]. Nevertheless, comprehensive investigations addressing the effects of processing variables

Accepted Manuscript

ACCEPTED MANUSCRIPT

on phase assemblage, particle morphology, chromatic properties, and glaze compatibility are still scarce.

A review of the available literature on $Ca_4Al_6CrO_{16}$ shows that research on this phase remains relatively sparse despite its favorable structural and thermal characteristics. Initial reports [21-23] established its cubic structure, thermal stability to approximately 1500 °C, and the characteristic yellow hue arising from Cr(VI) incorporation within the calcium aluminate lattice. Later studies [24-29] examined its phase-development pathway, dissolution kinetics, and environmental response, demonstrating that the phase retains high structural integrity and chemical inertness under oxidizing conditions. These features indicate that this oxide may have potential beyond conventional ceramic applications, including use in polymer-based coloration systems.

Given the presence of Cr(VI), its chemical stability and potential for chromium release are also important considerations for the safe application of this pigment. Regulatory guidelines have established strict limits for hexavalent chromium in drinking water due to its potential environmental and health impacts. For instance, the World Health Organization (WHO) recommends a maximum permissible concentration of 0.05 mg L^{-1} for Cr(VI) [26, 27], while earlier regulations by the United States Environmental Protection Agency (EPA) set a limit of 0.1 mg L^{-1} for total chromium [28].

The chemical stability of $Ca_4Al_6CrO_{16}$ in aqueous environments has been evaluated in the literature through inductively coupled plasma optical emission spectroscopy (ICP-OES) measurements of dissolved Ca, Al, and Cr ions. The reported solubility product constants (Ksp) of $Ca_4Al_6CrO_{16}$ in deionized water are extremely low, with values of 1×10^{-22}, 4.6×10^{-21}, and 2.4×10^{-20} at 12, 25, and 40 °C, respectively [22]. Such low Ksp

ACCEPTED MANUSCRIPT

values clearly indicate a negligible tendency for ion release and confirm the high chemical durability of this pigment in aqueous media.

The reported low solubility and limited chromium release of $Ca_4Al_6CrO_{16}$ indicate its high chemical durability and effective retention of Cr(VI) within its crystalline framework [22, 25]. These characteristics are particularly relevant to the safe application of Cr-containing pigments in coating and polymer systems. For $Ca_4Al_6CrO_{16}$ itself, the available literature has largely addressed structural and chemical characteristics rather than its broader pigment-related optical functionality. To the best of the authors' knowledge, no DFT-based investigation of this phase has been reported in the literature to date, and no combined experimental–theoretical study has yet been conducted.

Although experimental characterization provides essential information on the structural, optical, and colorimetric properties of pigments, it cannot always clarify the atomic-scale origin of their electronic and optical behavior. Complementary theoretical approaches are therefore useful for relating crystal structure to electronic states, orbital interactions, and magnetic properties. Among these approaches, first-principles methods such as density functional theory (DFT) provide an effective framework for investigating the electronic structure of inorganic materials.

Recent studies have demonstrated that DFT-based calculations can provide valuable insight into the electronic structure of transition-metal-containing oxides and the orbital interactions associated with their physical properties [30-32]. To complement the experimental characterization, first-principles DFT+U calculations were performed on the single-phase reference composition to elucidate the electronic structure, magnetic characteristics, and Cr–O orbital interactions of $Ca_4Al_6CrO_{16}$ and to provide a theoretical

ACCEPTED MANUSCRIPT

framework for interpreting the experimentally observed optical and colorimetric properties [11, 31-33].

The pigments were synthesized via a conventional solid-state route involving the mixing and milling of precursor oxides followed by high-temperature calcination [32, 34, 35]. The experimentally obtained materials were subsequently evaluated for structural characteristics and coloration performance, including their incorporation into polymer matrices.

The present study therefore combines experimental characterization with DFT+U calculations to elucidate the structural, electronic, and magnetic characteristics of $Ca_4Al_6CrO_{16}$ and to examine their relationship with the experimentally observed optical and colorimetric behavior.

The objective of the present study is to investigate the structural, optical, colorimetric, and electronic properties of Ca-Al-Cr oxide pigments based on the $Ca_4Al_6CrO_{16}$ phase and to evaluate their performance in polyurethane-based colored coatings. In this study, the term Ca-Al-Cr oxide refers to the synthesized crystalline $Ca_4Al_6CrO_{16}$-based pigment powder rather than elemental Ca, Al, or Cr nanoparticles. The synthesized pigment consists of crystalline oxide particles, with Cr incorporated into the calcium aluminate structure. To this end, a series of pigments with different Ca-Al precursor ratios and calcination temperatures (1100 and 1200 °C) were synthesized by the solid-state reaction method and characterized using XRD, Rietveld refinement, SEM, UV–Vis diffuse reflectance spectroscopy, and CIELAB colorimetry. The synthesized pigments were subsequently incorporated into polyurethane coatings to assess their practical coloration behavior. In parallel, DFT+U calculations were performed for the single-phase

ACCEPTED MANUSCRIPT

$Ca_4Al_6CrO_{16}$ composition to examine its electronic and magnetic properties. By integrating the experimental and computational results, this work aims to establish correlations among phase composition, microstructure, electronic structure, and color performance in $Ca_4Al_6CrO_{16}$-based pigment systems and to provide fundamental insight into their potential for durable polymer-coloration applications.

2. Experimental

2.1. Computational details

First-principles calculations were carried out within the DFT+U framework using the Quantum ESPRESSO package [36, 37]. The crystallographic structure of $Ca_4Al_6CrO_{16}$ was constructed based on experimental XRD data and validated crystallographic information obtained from the Crystallography Open Database (COD). Considering the relatively large number of atoms in the $Ca_4Al_6CrO_{16}$ crystal structure, a primitive unit cell consistent with the cubic crystal symmetry was adopted [38, 39] to significantly reduce the computational cost while preserving the essential structural and electronic characteristics of the material. The primitive unit cell employed in the DFT+U calculations contains 35 atoms: 4 Ca, 6 Al, 1 Cr, and 24 O atoms. Structural visualization and analysis of charge density and electron localization were performed using the VESTA software [40, 41].

Prior to the electronic structure calculations, full structural relaxation was carried out by optimizing both the lattice parameters and atomic positions using the Broyden–Fletcher–Goldfarb–Shanno (BFGS) algorithm until the total energy and atomic forces satisfied the convergence criteria of 1×10^{-5} Ry and 1×10^{-4} Ry $Bohr^{-1}$, respectively.

Accepted Manuscript

ACCEPTED MANUSCRIPT

Density functional theory (DFT) calculations were performed using the Quantum ESPRESSO package with the GGA-PBE exchange–correlation functional and PAW pseudopotentials. To properly account for the localized nature of the Cr 3d states, the DFT+U method was applied. The effective Hubbard parameter was determined using density functional perturbation theory (DFPT) [42], yielding U(Cr–3d) = 7.13 eV.

All calculations were performed using collinear spin polarization. The calculations were carried out using a 4 × 4 × 4 k-point mesh. The kinetic energy cutoffs for the wave functions and charge density were set to 90 and 900 Ry, respectively.

2.2. Materials

The starting materials employed in this work were chromium oxide (Cr_2O_3, 99.0% purity), aluminum oxide (Al_2O_3, 99.0% purity), and calcium carbonate ($CaCO_3$, 98.0% purity). All chemicals were obtained from a commercial supplier (Samchun Pure Chemical Co., Ltd., Republic of Korea) and were used as received without any additional purification.

2.3. Pigment preparation

The required amounts of $CaCO_3$, Al_2O_3, and Cr_2O_3 powders were determined and weighed based on the stoichiometric ratios given in Table 1. The raw materials were mixed in distilled water and homogenized for 1 h at ambient temperature using magnetic stirring. The resulting suspension was subsequently dried in a laboratory electric oven (SHIMIFAN, PID-controlled) for 15 h at 130 °C to obtain precursor powders. After drying, the powders were lightly ground using an agate mortar to ensure homogeneity

ACCEPTED MANUSCRIPT

and then calcined in air at 1100 or 1200 °C for 2 h using a laboratory electric furnace (FLE6-1500, 4.4 kW, single-phase). The heating schedule consisted of heating from room temperature to 300 °C within 30 min, followed by heating to 600 °C within an additional 30 min, and then heating to the final calcination temperature (1100 or 1200 °C) within 1 h. The samples were maintained at the final temperature for 2 h.

Upon completion of the calcination process, the samples were allowed to cool naturally to room temperature inside the furnace (Figure 1). The calcined products were then ground again using an agate mortar to obtain fine pigment powders suitable for dispersion in the polymer matrix. No sieving step was applied after the final grinding. The same manual grinding procedure using an agate mortar was applied to all pigment samples to minimize differences in powder preparation. The resulting pigments were subsequently used for the preparation of pigmented polyurethane films as described in Section 2.4.

Accepted Manuscript

2.4. Preparation of pigmented polyurethane films

A polyurethane (PU) resin solution was prepared by mixing PU resin with xylene at a weight ratio of 1:1 (100 wt.% xylene relative to the PU resin) under magnetic stirring for 3 min. Each pigment sample (LY_1-LY_6) was then incorporated at 35 wt.% relative to the PU resin and dispersed for 5 min to achieve a homogeneous suspension. Subsequently, N75 curing agent (40 wt.% relative to the PU resin) was added, and the mixture was further stirred for 3 min. The resulting pigmented polyurethane formulations were deposited onto clean glass substrates by solution casting and allowed to dry and cure at room temperature for 24 h.

ACCEPTED MANUSCRIPT

Table 1. Molar ratios of starting compounds and calcination temperature.

pigment	Al_2O_3	$CaCO_3$	Cr_2O_3	T(°C)
LY_1	6		1	1200
LY_2	6	8	1	1100
LY_3	7	9	1	1200
LY_4	8	10	1	1200
LY_5	10	12	1	1200
LY_6	10	12	1	1100

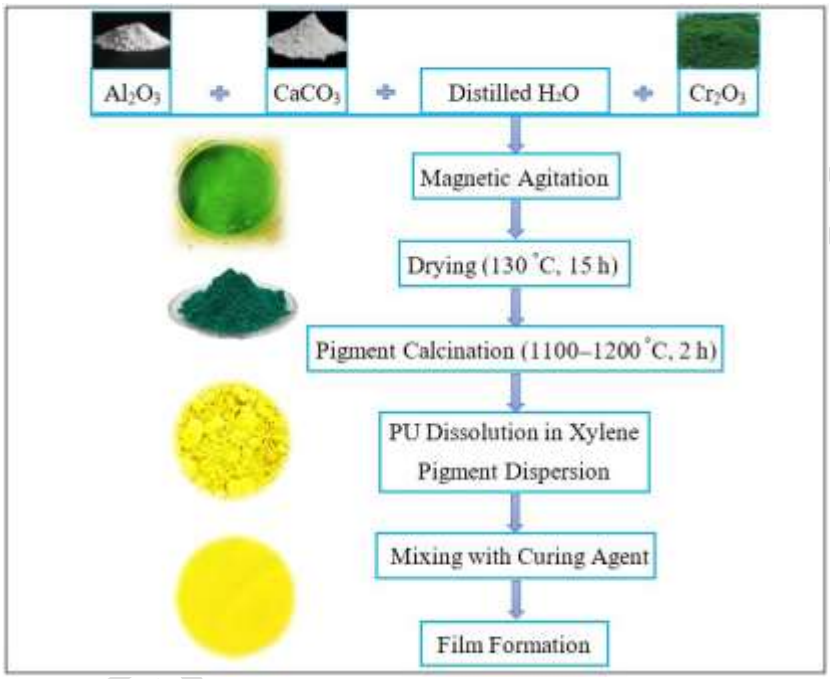


Figure 1. Pigment synthesis process, dispersion within polymer matrix and coating application

2.5. Characterization

The synthesized pigment was characterized in terms of its morphology by scanning electron microscopy (SEM; TESCAN Mira III) at an accelerating voltage of 30 kV. Particle size distributions were obtained by analyzing the SEM images with Digimizer software. The crystalline phases and structural features of the samples were examined by XRD using Cu Kα X-ray radiation with a wavelength of 1.54060 Å. Using the θ–2θ scanning geometry, XRD measurements were performed under an operating voltage of 36 kV and a current of 36 mA on a D8 Advance diffractometer manufactured by Bruker

ACCEPTED MANUSCRIPT

(Germany). The crystal structure of $Ca_4Al_6CrO_{16}$ was visualized and modeled using VESTA software [40, 41].

The optical response of the pigment was assessed with a UV–Vis spectrometer (UVS-2500 miniature spectrometer, Phystec, Iran). Diffuse reflectance spectra were collected within the 390-740 nm wavelength interval, and the corresponding L*, a*, and b* color coordinates were obtained. According to the CIELAB system, L* indicates lightness, whereas a* and b* describe the red–green and yellow–blue coordinates, respectively. The chroma (C*), used to express color saturation, was calculated from $C^* = [(a^*)^2 + (b^*)^2]^{1/2}$. The hue angle (h°), which indicates the dominant color tone, was determined using $h° = \tan^{-1}(b^*/a^*)$.

A uniform-deformation Williamson–Hall (W–H) approach was employed to estimate the average crystallite dimension together with the associated lattice microstrain [43]. The analysis assumes that the observed broadening of the XRD reflections originates from both crystallite-size effects and microstrain. These two contributions were separated using the following equation (Eq. 1):

$$\beta \cos\theta = \frac{k\lambda}{D} + 4\varepsilon \sin\theta \qquad (1)$$

In this relation, the diffraction peak broadening at half of its maximum intensity is denoted by β, while θ corresponds to the Bragg diffraction angle. The symbols λ, D, and ε refer to the incident X-ray wavelength, crystallite dimension, and lattice microstrain, respectively. The W–H calculations were performed using X'Pert HighScore software.

3. Results and Discussion

ACCEPTED MANUSCRIPT

3.1. Structural properties

3.1.1. Microstructure

SEM analysis was conducted to examine the morphological characteristics of the pigment powders for all six samples used in the polymer study (Figure 2), and the associated histograms depicting the particle-size distributions are provided in Figure 3. Figure 2 shows that the pigment particles, while irregular, generally approximate spherical or ellipsoidal shapes. Their surfaces vary from smooth to noticeably rough. Agglomeration is observed, potentially due to particle adhesion or van der Waals forces.

ACCEPTED MANUSCRIPT

ACCEPTED MANUSCRIPT

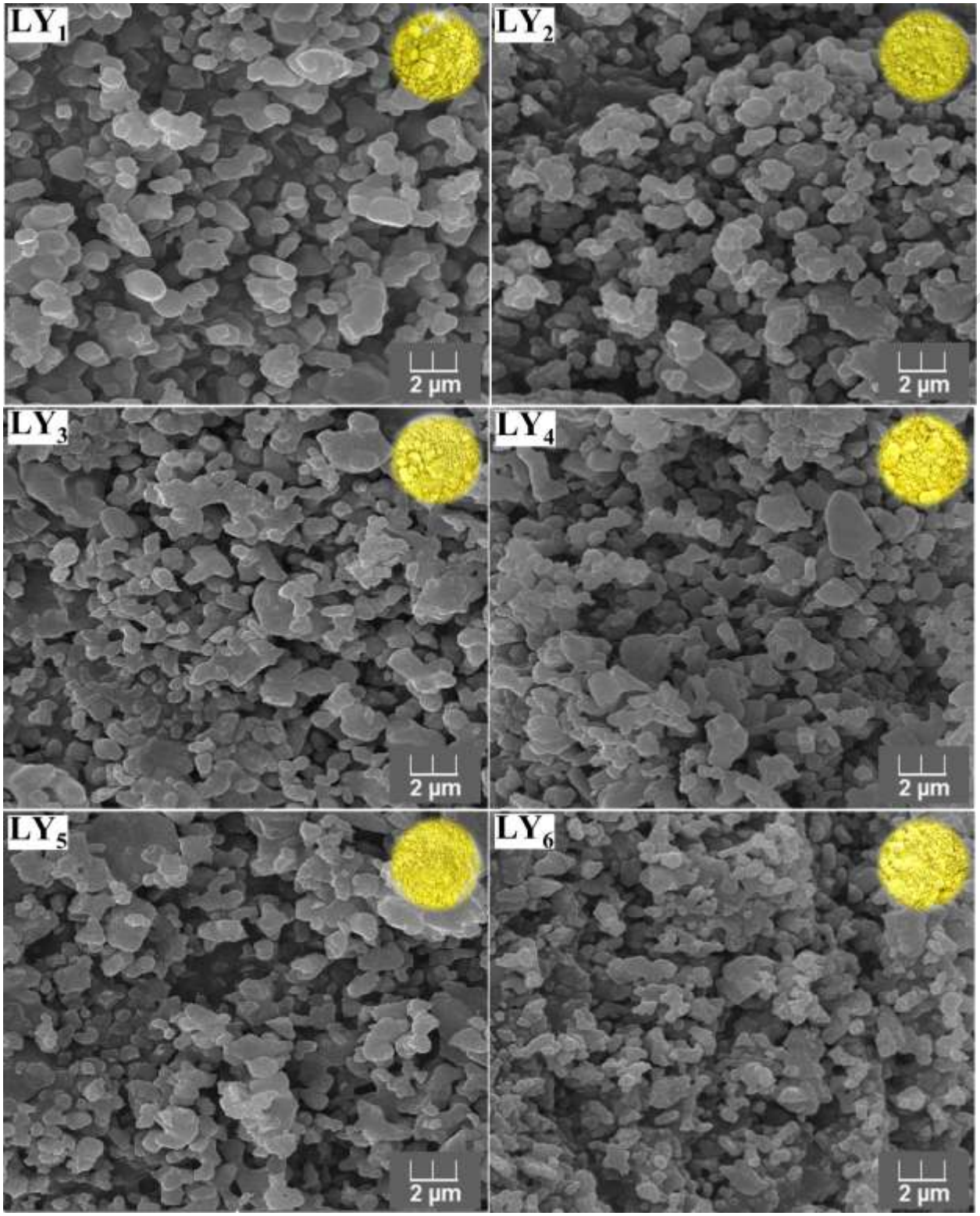


Figure 2. SEM images of the synthesized pigments (LY_1–LY_6), illustrating their particle morphology, size distribution, and degree of agglomeration.

ACCEPTED MANUSCRIPT

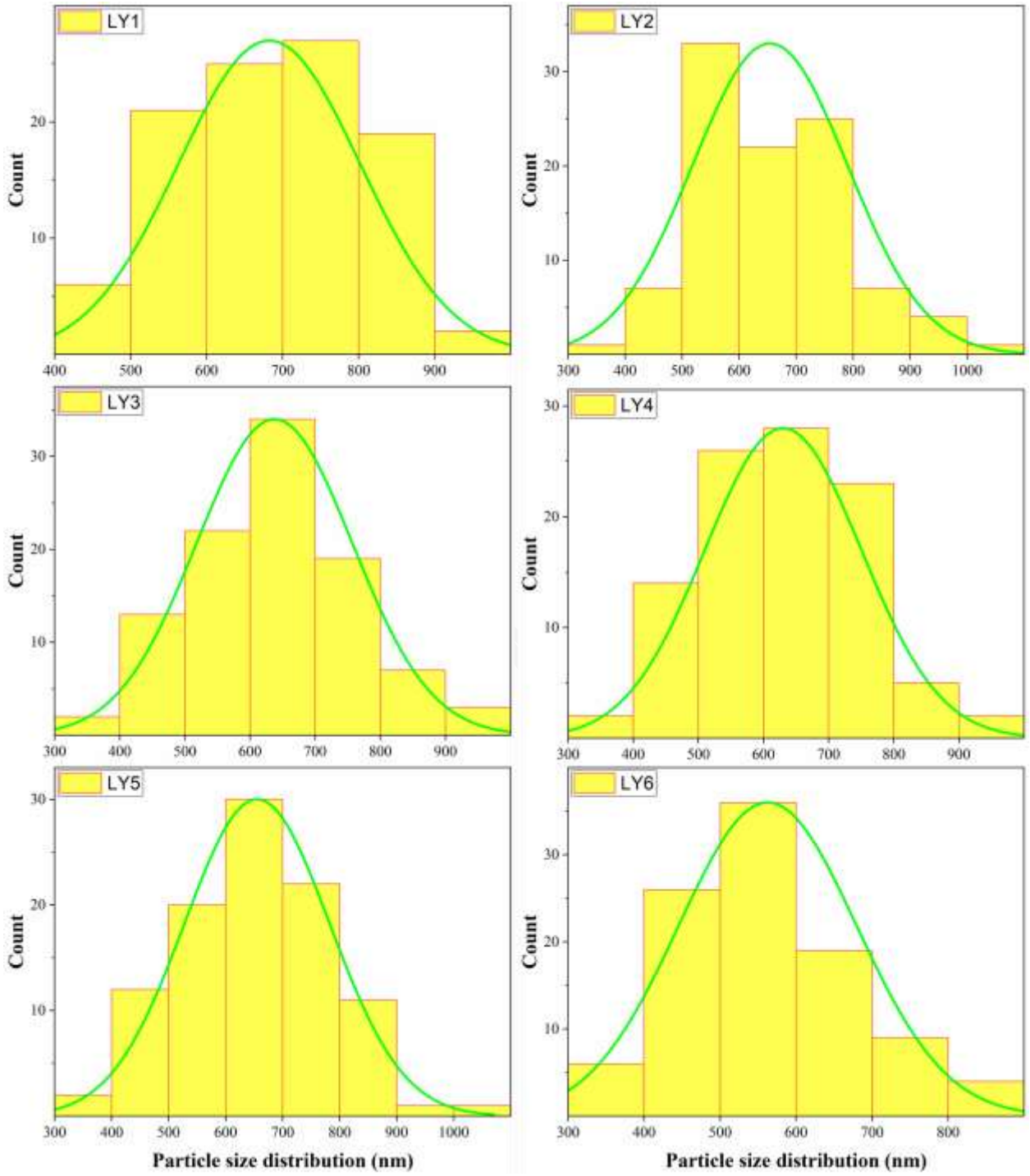


Figure 3. Particle size histograms for pigments LY_1–LY_6.

Table 2 summarizes the mean particle dimension along with the upper and lower particle-size limits for the pigments. For particle size determination, large agglomerates

ACCEPTED MANUSCRIPT

and obvious particle clusters were excluded from the analysis to better represent the size of individual pigment particles. For each sample, the statistical analysis was performed based on measurements of 100 randomly selected particles. The particle size data in Table 2 show that the average particle sizes of all pigment samples range from 563 to 682 nm, while their median sizes range from 553 to 696 nm. Both measures indicate that the pigment particles are within the submicron range, which is relevant to their incorporation into polymer matrices.

The particle size results indicate that LY_1 and LY_2 (later shown to be single-phase) possess approximately the largest particle sizes. Among the samples calcined at 1200 °C, LY_4 has the smallest mean particle dimension and, as will be explained subsequently, displays enhanced color performance compared with the other pigments prepared in this and the previous study, as well as with certain commercial samples [6, 44, 45].

For the pigments calcined at 1200 °C, a clear trend can be observed from LY_1 to LY_3: as the molar ratios of aluminum oxide and calcium carbonate in the starting compositions increase, the particle size gradually decreases. A similar reduction in particle size is also observed from LY_3 to LY_4 with further increases in the molar ratios of these two components. However, this trend does not continue from LY_4 to LY_5. Overall, among all samples calcined at 1200 °C, LY_4 exhibits the smallest particle size.

This distinctive behavior of LY_4 suggests that the final microstructure is governed by the combined influence of composition and calcination temperature, indicating that optimal particle refinement is strongly dependent on the starting composition. Changes in particle size upon calcination cannot be explained exclusively by thermal effects; rather, they result from the interplay of structural transformations, particle coalescence during

Accepted Manuscript

ACCEPTED MANUSCRIPT

sintering, and variations in chemical composition associated with different Ca-Al-Cr molar proportions [33, 46]. These variations in particle size and distribution can markedly affect the pigments' optical characteristics, dispersion properties, and stability over extended periods, as elaborated in subsequent sections.

Table 2. Particle size measurements of samples LY_1-LY_6.

pigments	Minimum particle size (nm)	Maximum particle size (nm)	Average particle size (nm)	Median particle size (nm)
LY_1	426	936	682	696
LY_2	378	1085	654	640
LY_3	377	939	637	636
LY_4	373	964	630	633
LY_5	377	1023	655	654
LY_6	345	884	563	553

3.1.2. Crystal structure analysis

3.1.2.1. XRD analysis

The structural characteristics of the synthesized pigments were first assessed by X-ray diffraction, with the XRD patterns of LY_1-LY_6 shown in Figure 4. The diffraction peaks of LY_1 are in close correspondence with the reference pattern of $Ca_4Al_6CrO_{16}$ (ICDD No. 96-900-4870; COD entry No. 9004869), confirming $Ca_4Al_6CrO_{16}$ as the crystalline phase of LY_1. The main reflection occurs at $2\theta \approx 23.66°$, which is consistent with the cubic $Ca_4Al_6CrO_{16}$ structure. The crystal structure is characterized by equal lattice constants of 9.223 Å along all three axes ($a = b = c$), with the interaxial angles fixed at 90° ($\alpha = \beta = \gamma$).

The phase constitution obtained for the different compositions provides additional information on the structural evolution of the pigment series. The XRD patterns show that LY_1 and LY_2 are single-phase $Ca_4Al_6CrO_{16}$ pigments. For LY_3, $Ca_4Al_6CrO_{16}$ remains the major phase, accompanied by a minor amount of monoclinic $CaAl_2O_4$ (COD

ACCEPTED MANUSCRIPT

9013917). In LY_4–LY_6, $CaAl_2O_4$ (COD 2002888, monoclinic) is likewise detected as a secondary phase together with the $Ca_4Al_6CrO_{16}$ host structure. Thus, the compositions exhibit a systematic transition from nearly single-phase materials to $Ca_4Al_6CrO_{16}$-containing multiphase systems.

The predominance of $Ca_4Al_6CrO_{16}$ is particularly relevant to the color development of these materials because this phase contains the Cr(VI) chromophore responsible for the pronounced yellow hue. The secondary $CaAl_2O_4$ phase is chromophore-free and therefore does not directly generate the yellow color, although its presence may modify the overall optical response through its influence on brightness and particle dispersion. The colorimetric results discussed later indicate that incorporation of this secondary phase is associated with a shift from the greenish-yellow appearance toward a more pronounced yellow hue [10].

The formation of $Ca_4Al_6CrO_{16}$ is reported to initiate at approximately 900 °C, while its highest degree of crystallinity is achieved around 1100 °C. The compound preserves its cubic crystal structure over a wide temperature range up to about 1500 °C, as evidenced by high-temperature XRD analyses that reveal no noticeable peak shifts or emergence of secondary phases. At temperatures exceeding 1500 °C, the disappearance of the characteristic diffraction peaks indicates the onset of structural instability, likely due to phase transformation or thermal decomposition [21, 22]. Zhang et al. [23] reported that pure $Ca_4Al_6CrO_{16}$ exhibits a greenish–yellow hue under unpolarized light and is composed of polyhedral particles; the corresponding colorimetric parameters of this greenish-yellow pigment are presented in the following sections. They also determined a refractive index of approximately 1.655 and a density of about 2.67 gcm^{-3}, while

Accepted Manuscript

ACCEPTED MANUSCRIPT

demonstrating that the material retains its structural stability at temperatures above 1500 °C.

The selection of the calcination temperatures used in the present study was guided by both previous experimental observations and the reported thermal behavior of $Ca_4Al_6CrO_{16}$. In our previous investigation [6], a comparative analysis of synthesis temperatures revealed that samples prepared at 1200 °C exhibited improved CIELAB colorimetric performance compared with those synthesized at higher temperatures. Together with the reported maximum crystallinity near 1100 °C [21, 22], these findings motivated the use of 1100 and 1200 °C for the six pigment compositions investigated here [25].

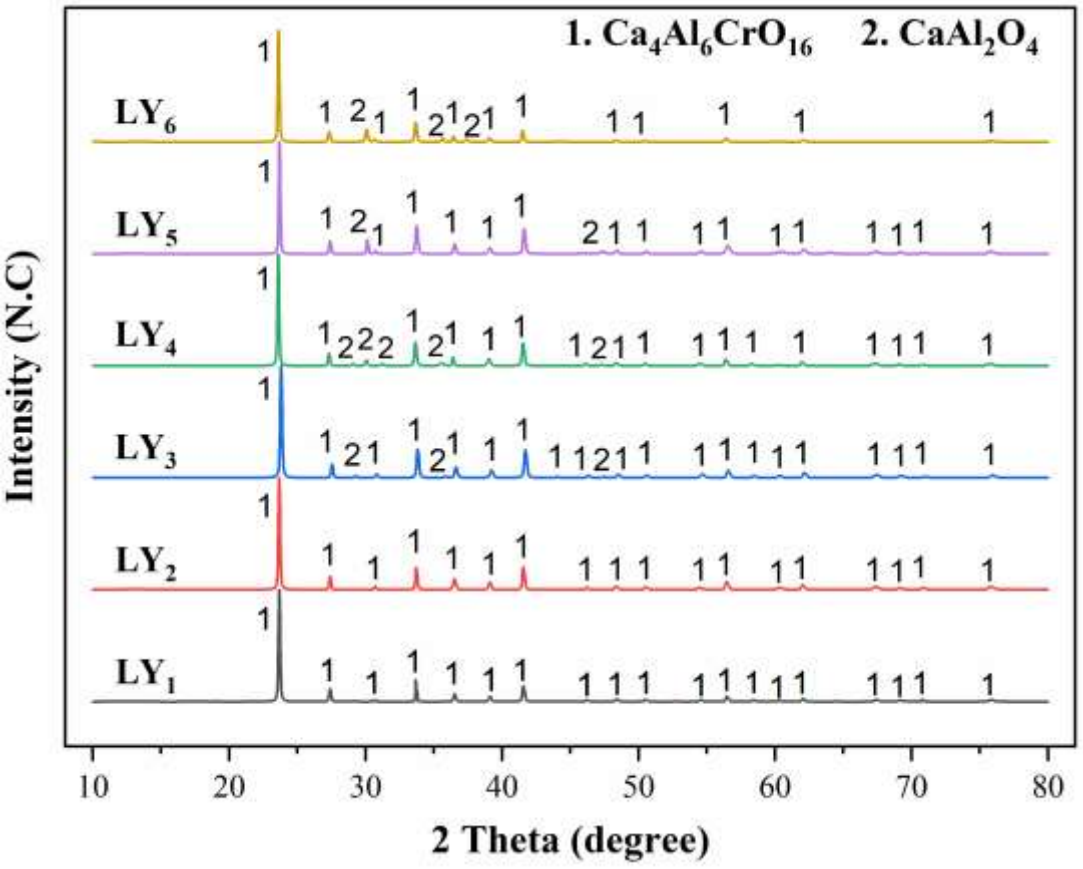


Figure 4. X-ray diffraction patterns recorded for pigments LY_1–LY_6.

ACCEPTED MANUSCRIPT

The LY_1 sample was prepared under optimized conditions to favor the formation of $Ca_4Al_6CrO_{16}$ with negligible secondary-phase contribution. This high phase purity provides a suitable structural basis for correlating the experimental optical response with the electronic-structure calculations presented later. As demonstrated in our previous studies [6], $Ca_4Al_6CrO_{16}$ is the chromophore-containing phase that primarily contributes to the yellow hue, even in multiphase systems. Hexavalent chromium (Cr^{6+}) serves as the principal chromophore and, as discussed in subsequent sections [47], plays a crucial role in the development of the pigment's color.

Precise regulation of precursor composition and thermal treatment is therefore important for obtaining the desired phase assemblage and chromatic response [48-50]. Under the conditions employed here, LY_1 predominantly crystallized as $Ca_4Al_6CrO_{16}$, in accordance with the reported stability of this phase within the CaO-Al_2O_3-Cr_2O_3 system. The very small contribution of additional calcium-aluminate phases enhances the phase purity relative to previously reported multiphase compositions and facilitates comparison between the experimentally observed behavior and the theoretical results. Although literature reports based on XPS measurements indicate that chromium in this structure is primarily present in the hexavalent state [22], definitive determination of the Cr crystallographic site and local coordination would require site-sensitive methods such as XANES/EXAFS or high-resolution Rietveld occupancy refinement; these measurements are beyond the scope of the present study and are therefore left for future work.

The Williamson–Hall (W–H) approach [43] was employed to assess the crystallite size and microstrain of the synthesized pigments. Unlike the Scherrer equation, which treats diffraction-line broadening as a size-related effect only, the W-H method accounts

Accepted Manuscript

ACCEPTED MANUSCRIPT

for both crystallite-size and strain-induced broadening of the diffraction lines. The resulting crystallite-size and microstrain values are listed in Table 3. Because the W-H method provides semi-quantitative estimates rather than highly precise structural parameters, the calculated crystallite sizes were reported after rounding to the nearest nanometer.

Table 3. Williamson–Hall-derived crystallite sizes.

Pigment	Crystallite Size (nm)	Microstrain ($\times 10^{-3}$)
LY_1	88	0.60
LY_2	106	0.95
LY_3	73	0.82
LY_4	69	0.45
LY_5	104	1.01
LY_6	82	0.61

For each pigment, the crystallite size (D) and lattice strain (ε) were extracted from the intercept and slope of the linear βcosθ versus 4sinθ relationship, respectively. The corresponding fitting procedure is exemplified by the W–H plot obtained for LY_1 in Figure 5. The crystallite size of LY_2 was estimated to be about 106 nm, while its microstrain was calculated as 0.95×10^{-3}, representing the highest value among the investigated samples. This relatively large strain contribution indicates that lattice distortion plays an appreciable role in the diffraction-line broadening of LY_2.

ACCEPTED MANUSCRIPT

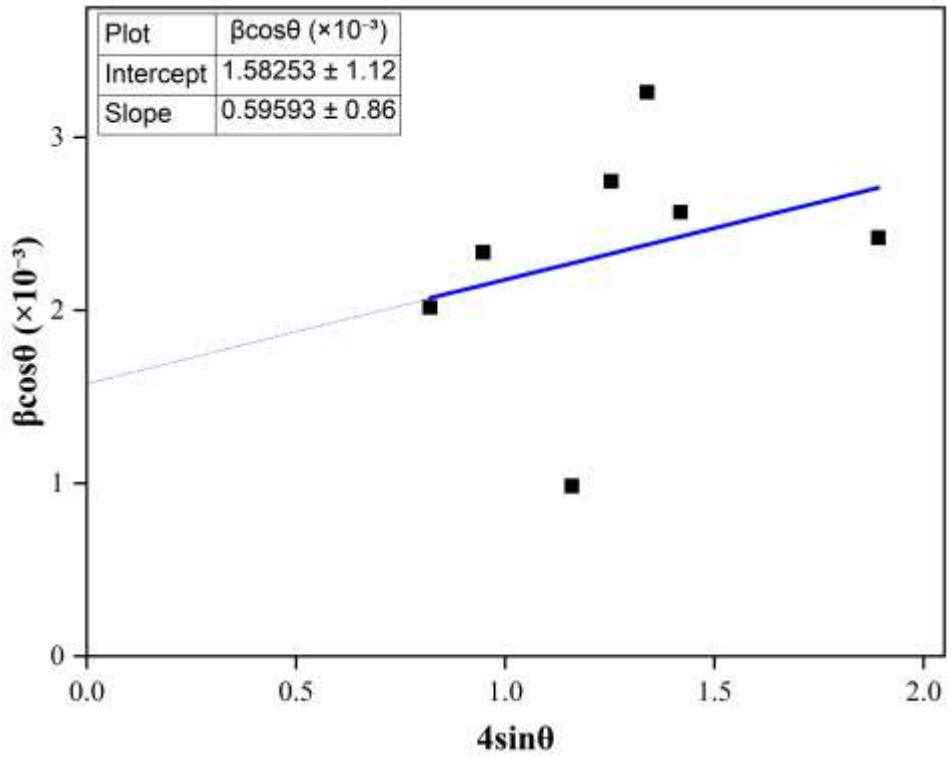


Figure 5. Williamson–Hall analysis for crystallite size and microstrain in $Ca_4Al_6CrO_{16}$ (LY_1) pigment.

A different behavior was obtained for LY_4, which showed the smallest crystallite size (69 nm) but also the lowest microstrain (0.45×10^{-3}). The latter result implies that lattice distortion makes a comparatively minor contribution to the peak broadening of LY_4, although its small crystallite dimensions remain an important broadening factor. The lower microstrain of LY_4 therefore reflects a smaller degree of lattice distortion relative to the other samples and should be interpreted together with its crystallite size and other structural characteristics.

Among the pigments calcined at 1200 °C (LY_1, LY_3, LY_4, and LY_5), the mean particle size decreased sequentially from 682 nm in LY_1 to 637 nm in LY_3 and 630 nm in LY_4, followed by an increase to 655 nm in LY_5. The crystallite sizes estimated from the

ACCEPTED MANUSCRIPT

Williamson–Hall analysis showed a similar numerical trend, decreasing from 88 nm (LY_1) to 73 nm (LY_3) and 69 nm (LY_4), and then increasing to 104 nm for LY_5. These particle-size and crystallite-size results are presented separately in Tables 2 and 3, respectively.

3.1.2.2. Structural characterization using VESTA and rietveld analysis

VESTA was used to inspect the three-dimensional arrangement of the $Ca_4Al_6CrO_{16}$ structure (Figure 6) [40, 41], whereas quantitative phase fractions were obtained by Rietveld refinement of the XRD patterns using MAUD [51]. The refinement outputs are shown in Figure 7 and summarized in Table 4, including the phase composition, weight fractions, and lattice parameters of all synthesized pigments.

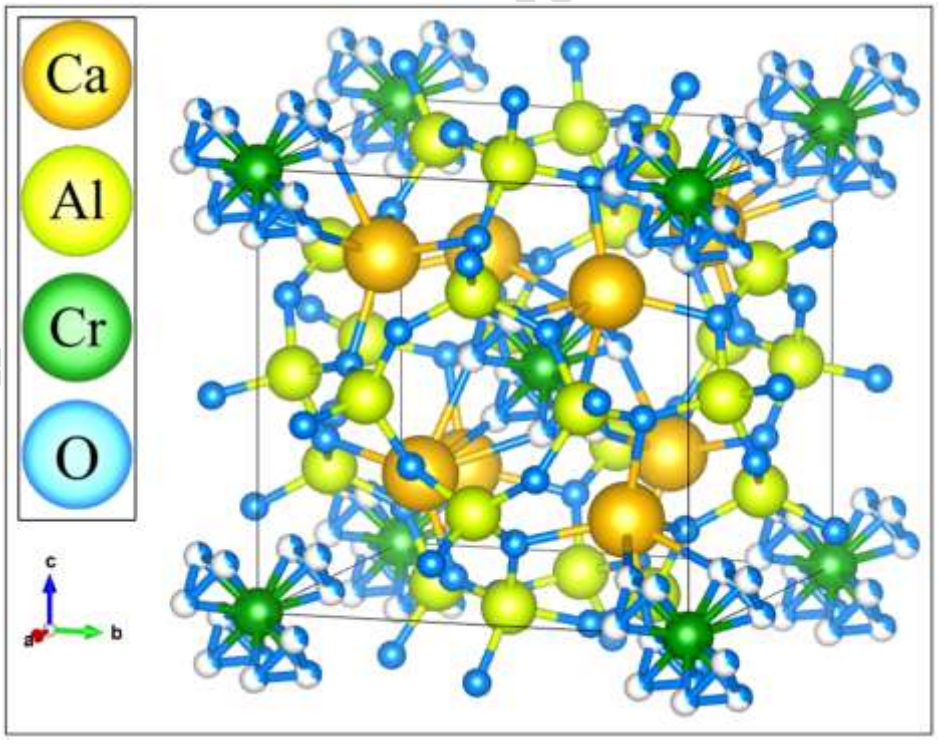


Figure 6. Crystal structure of the $Ca_4Al_6CrO_{16}$ phase displayed using VESTA software.

ACCEPTED MANUSCRIPT

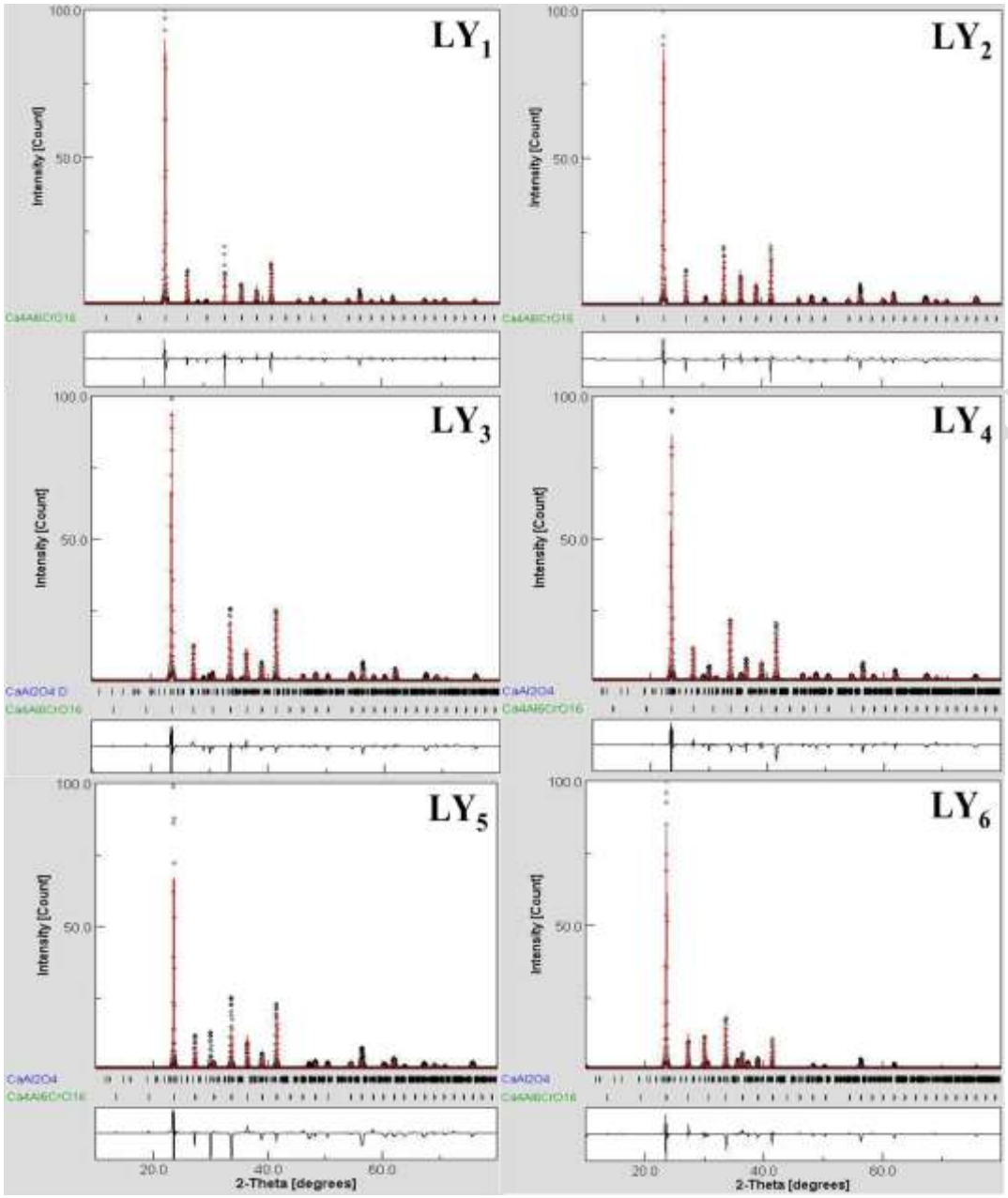


Figure 7. Rietveld-refined XRD patterns of samples LY_1-LY_6.

According to the XRD analysis results and stoichiometric relationships listed in Table 5, samples LY_1 and LY_2 can be considered nearly single-phase, whereas LY_3 to LY_6 contain $CaAl_2O_4$ as a secondary phase in addition to the main $Ca_4Al_6CrO_{16}$ phase. The refinement outcomes are illustrated in Figure 7 and compiled in Table 4, where the phase

ACCEPTED MANUSCRIPT

composition, weight fractions, and lattice parameters of all prepared pigments are reported. The parameter σ (sig) represents the accuracy of the refinement process, and ideally its value should be lower than 2. In the present case, all samples exhibit σ values of approximately 0.3, indicating a high level of refinement accuracy. Furthermore, the obtained structural parameters are very close to those of the reference COD data.

Table 4. Pigment phases, wt.%, reference codes, and lattice parameters.

Sample	Phases	Weight Fraction%	Reference Code	sig	Lattice Parameters (Å)					
					a(Å)	b(Å)	c(Å)	α(◦)	β(◦)	ϒ(◦)
LY_1	$Ca_4Al_6CrO_{16}$	100	96-900-4870	0.236	9.223	9.223	9.223	90	90	90
	$CaAl_2O_4$	0	-	-	-	-	-	-	-	-
LY_2	$Ca_4Al_6CrO_{16}$	100	96-900-4870	0.269	9.223	9.223	9.223	90	90	90
	$CaAl_2O_4$	0	-	-	--	-	-	-	-	-
LY_3	$Ca_4Al_6CrO_{16}$	98.8	96-900-4870	0.282	9.223	9.223	9.223	90	90	90
	$CaAl_2O_4$	1.20	96-901-3918		7.972	8.628	10.26	90	94	90
LY_4	$Ca_4Al_6CrO_{16}$	81.7	96-900-4870	0.271	9.223	9.223	9.223	90	90	90
	$CaAl_2O_4$	18.3	96-200-2889	-	8.700	8.092	17.48	90	119.7	90
LY_5	$Ca_4Al_6CrO_{16}$	96.7	96-900-4870	0.426	9.223	9.223	9.223	90	90	90
	$CaAl_2O_4$	3.30	96-200-2889	-	8.700	8.092	17.48	90	119.7	90
LY_6	$Ca_4Al_6CrO_{16}$	71.0	96-900-4870	0.250	9.223	9.223	9.223	90	90	90
	$CaAl_2O_4$	29.0	96-200-2889	-	8.700	8.092	17.48	90	119.7	90

In earlier studies, where secondary calcium aluminate phases such as $CaAl_2O_4$ coexisted with the chromophore-bearing $Ca_4Al_6CrO_{16}$ phase, variations in hue and brightness were attributed to both optical dilution effects and localized distortions arising near phase boundaries [6]. In the present work, the XRD results demonstrate that the LY_1 composition was intentionally designed to obtain a predominantly single-phase $Ca_4Al_6CrO_{16}$ pigment with negligible secondary phases. Therefore, the observed greenish–yellow coloration of LY_1 can be mainly assigned to intrinsic electronic transitions associated with Cr^{6+} species within the $Ca_4Al_6CrO_{16}$ lattice. Although

ACCEPTED MANUSCRIPT

literature reports based on XPS measurements indicate that chromium in this structure is primarily present in the hexavalent state [22], a definitive identification of Cr site occupancy and local coordination would require element-specific techniques such as XANES/EXAFS or high-resolution Rietveld occupancy refinement. Such analyses fall beyond the scope of the present work but are proposed for future studies.

In this study, the initial molar ratios were deliberately selected for LY_1 to favor the formation of single-phase $Ca_4Al_6CrO_{16}$ under solid-state reaction conditions while accounting for Ca loss during the thermal breakdown of $CaCO_3$ and variations in the reactivity of the starting precursors. A similar stoichiometric design was adopted for LY_2, which also resulted in an almost single-phase composition. The balanced reaction equations and the predicted mass fractions of $Ca_4Al_6CrO_{16}$ for all compositions (LY_1–LY_6) are summarized in Table 5, providing a unified stoichiometric framework for the entire experimental series. Consistent with these stoichiometric predictions, the XRD analysis revealed exactly the expected phase assemblage, confirming the formation of the phases anticipated from the balanced reaction equations.

For compositions containing secondary phases, the theoretical phase proportions were evaluated using molar-mass calculations. The molar masses of $Ca_4Al_6CrO_{16}$ and $CaAl_2O_4$ are approximately 630.2 and 158.04 $g \cdot mol^{-1}$, respectively. Using the stoichiometric coefficients listed in Table 5, the expected mass fractions for LY_4 are about 80 wt% and 20 wt.%, respectively. These values are in very good agreement with the Rietveld refinement results for LY_4 (Table 4), where the $Ca_4Al_6CrO_{16}$ phase was quantified at 81.7 wt.%, confirming the consistency between the stoichiometric predictions and experimental phase analysis. These results confirm that the phase assemblage observed

ACCEPTED MANUSCRIPT

experimentally is consistent with the designed precursor stoichiometry.

Precise control of precursor composition and calcination parameters plays a key role in achieving strong chromatic response and color stability [48-50]. However, for the other compositions, the agreement between stoichiometric predictions and Rietveld-derived phase fractions is not always exact, which is expected for complex solid-state reactions. Variations in precursor reactivity, diffusion kinetics, and local compositional fluctuations during calcination can lead to deviations between theoretical phase proportions and experimentally refined values. For example, in the case of LY_3, during solid-state synthesis the effective stoichiometry tends to shift toward $Ca_4Al_6CrO_{16}$ because of partial $CaCO_3$ decomposition, minor alumina volatilization, and the preferential incorporation of chromium into the Ca-Al-O lattice. As a result, an almost single-phase $Ca_4Al_6CrO_{16}$ composition (≈99 wt.%) was obtained for LY_3 under optimized firing conditions, in agreement with its thermodynamic stability in the CaO-Al_2O_3-Cr_2O_3 system.

Overall, while LY_1 served as the reference composition for first-principles calculations, the complete LY_1-LY_6 series enabled a systematic experimental investigation of phase evolution and polymer coloration performance across different stoichiometries.

Table 5. Stoichiometry and chemical reaction equations in pigments.

n	Equations		wt.% $Ca_4Al_6CrO_1$	pigments
1	$6Al_2O_3+8CaCO_3+Cr_2O_3+3/2O_2$	$\rightarrow 2Ca_4Al_6CrO_{16}+8CO_2$	100	LY_1-LY_2
2	$7Al_2O_3+9CaCO_3+Cr_2O_3+3/2O_2$	$\rightarrow 2Ca_4Al_6CrO_{16}+CaAl_2O_4+9CO_2$	88.9	LY_3
3	$8Al_2O_3+10CaCO_3+Cr_2O_3+3/2O_2$	$\rightarrow 2Ca_4Al_6CrO_{16}+2CaAl_2O_4+10CO_2$	80.0	LY_4
4	$10Al_2O_3+12CaCO_3+Cr_2O_3+3/2O_2$	$\rightarrow 2Ca_4Al_6CrO_{16}+4CaAl_2O_4+12CO_2$	66.6	LY_5 -LY_6

ACCEPTED MANUSCRIPT

3.1.3. Structural stability and chromium immobilization

According to Wu et al. [24], formation of the $Ca_4Al_6CrO_{16}$ phase is favored at temperatures above 1100 °C through the reaction of $(Al_{1-x}Cr_x)_2O_3$ intermediates with $CaCO_3$ under oxidizing conditions [25]. This formation pathway supports the incorporation of chromium into the calcium aluminate framework rather than its precipitation as an independent chromium oxide phase, leading to the development of $Ca_4Al_6CrO_{16}$ as the chromophore-bearing phase responsible for the characteristic coloration.

Semi-quantitative EDS analyses have shown an atomic chromium content of approximately 6.34% within the $Ca_4Al_6CrO_{16}$ lattice [25]. X-ray photoelectron spectroscopy further confirms that chromium is present exclusively in the hexavalent oxidation state [22], which is directly responsible for the observed yellow coloration. Moreover, this phase exhibits excellent thermal stability in air up to about 1500 °C [22, 25], underscoring its suitability for high-temperature pigment applications.

To further support the phase assignment and chemical composition of $Ca_4Al_6CrO_{16}$, previously published EDS results reported by Xu et al. [25] were considered. The reported elemental composition comprises Al (34.27 wt.%), Ca (18.58 wt.%), Cr (6.34 wt.%), and O (40.82 wt.%). These values are consistent with the nominal stoichiometry of $Ca_4Al_6CrO_{16}$ within the expected uncertainty of EDS analysis and support the incorporation of chromium into the calcium aluminate lattice. Furthermore, these literature-derived results are consistent with the XRD identification of the single-phase $Ca_4Al_6CrO_{16}$ composition obtained for LY_1 in the present study.

Kinetic analyses further revealed that the dissolution behavior follows a chemically

ACCEPTED MANUSCRIPT

controlled shrinking-core model, for which the activation energy was estimated to be 58.8 kJ mol^{-1}, further supporting the strong retention of Cr(VI) within the $Ca_4Al_6CrO_{16}$ crystal framework [22, 25]. These leaching characteristics were previously established [22] using a solid-state preparation procedure identical to that employed in the present work; consequently, additional leaching experiments were not performed here. Complementary studies have also identified Cr(VI) within the $Ca_4Al_6CrO_{16}$ structure by XRD analysis and demonstrated that chromium release remains well below environmentally critical thresholds [29].

Taken together, the combination of extremely low solubility, high thermal robustness, and compliance with established safety limits strongly supports that $Ca_4Al_6CrO_{16}$ is a chemically stable and environmentally safe yellow pigment for advanced coating and polymer applications.

3.1.4. Structural stability and magnetic properties

The magnetic moments calculated within the DFT+U framework indicate that the magnetic behavior of $Ca_4Al_6CrO_{16}$ is dominated by the chromium atoms. The total magnetization of the unit cell was calculated to be 8.00 μB/cell, indicating a spin-polarized ground state for $Ca_4Al_6CrO_{16}$. The Cr site exhibits a magnetic moment of approximately 3.44 μB, whereas Ca and Al atoms contribute negligibly to the total magnetization (Table 6). Small induced magnetic moments are observed on the oxygen atoms due to Cr–O hybridization. The oxygen atoms occupy two crystallographically nonequivalent sites (represented in Figure 6 by the fully blue oxygen spheres (O_1) and the blue–white oxygen spheres coordinated to Cr atoms (O_2)), exhibiting average magnetic

ACCEPTED MANUSCRIPT

moments of approximately -0.022 and +0.299 μB, respectively. The larger positive magnetic moment associated with the O_2 site is consistent with a stronger influence of the neighboring Cr atoms on its local electronic structure. These results are consistent with the PDOS analysis, which shows that the electronic states near the Fermi level are primarily associated with Cr 3d and O 2p orbitals. The calculated magnetic configuration therefore confirms that chromium is the principal source of the spin-polarized electronic structure of $Ca_4Al_6CrO_{16}$, while the oxygen atoms participate through Cr-O orbital hybridization. The finite total magnetization indicates a ferromagnetically polarized ground state. The magnetic behavior originates predominantly from the localized Cr 3d electrons, whereas Ca and Al contribute negligibly to the overall magnetization. The induced magnetic moments on the oxygen atoms further suggest magnetic coupling mediated through Cr–O interactions.

Table 6. Calculated magnetic moments (μB/atom) of $Ca_4Al_6CrO_{16}$.

Atom	Magnetic moment (μB/atom)
Cr	3.4406
Ca (average)	0.0025
Al (average)	0.0003
O_1 (12-23 average)	-0.0221
O_2 (24-35 average)	0.2985

The cohesive energy was calculated using Eq. 2 from the difference between the total energy of the optimized bulk structure and the energies of the isolated constituent atoms [52, 53]. The obtained cohesive energy is approximately -5.64 eV atom^{-1}, indicating strong interatomic bonding and confirming the thermodynamic stability of the $Ca_4Al_6CrO_{16}$ structure.

$$E_{coh} = \frac{E_{bulk} - \sum_N E_{iso}}{N}. \quad (2)$$

ACCEPTED MANUSCRIPT

3.2. Electronic structure analysis (DFT)

The spin-polarized electronic band structure and density of states (DOS) of $Ca_4Al_6CrO_{16}$ were calculated within the PBE+U framework and referenced to the Fermi level ($E_F = 0$). The band dispersion was evaluated along the high-symmetry k-path of the first Brillouin zone. The absolute Fermi energy of the optimized structure was calculated to be 5.019 eV; however, all energies are referenced to $E_F = 0$ for clarity (Figure 8).

The calculated electronic structure exhibits a pronounced spin dependence. While the spin-down channel shows a finite separation between occupied and unoccupied states, several spin-up bands cross or lie very close to the Fermi level. Consequently, the overall electronic structure does not display a well-defined band gap at E_F and may be described as a nearly gapless spin-polarized system within the PBE+U approximation. This behavior highlights the strong influence of Cr-derived electronic states on the electronic structure of $Ca_4Al_6CrO_{16}$. The pronounced difference between the spin-up and spin-down channels arises from exchange splitting of the Cr 3d states. As a consequence, the electronic states are shifted differently in the two spin channels, leading to an asymmetric spin-resolved electronic structure.

Although the spin-down channel exhibits a finite separation between occupied and unoccupied states, the presence of spin-up states crossing the Fermi level results in an overall zero-gap electronic structure when both spin channels are considered together. Such behavior is characteristic of a half-metallic ferromagnet, where one spin channel is metallic while the other exhibits semiconducting behavior.

ACCEPTED MANUSCRIPT

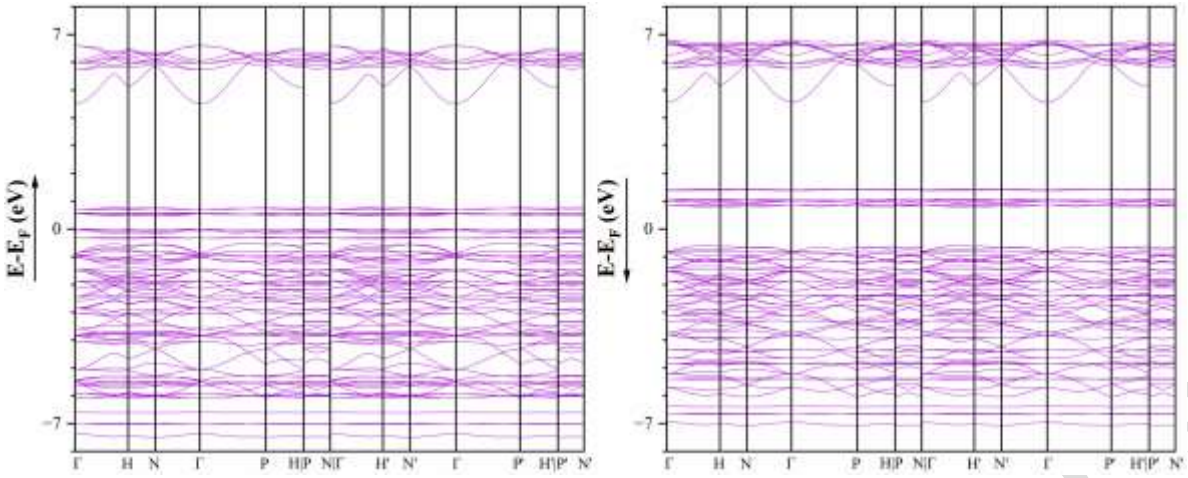


Figure 8. Spin-polarized electronic band structures of $Ca_4Al_6CrO_{16}$ calculated within the PBE+U approach, shown for (a) spin-up and (b) spin-down channels.

The total DOS analysis is consistent with the band-structure results and reveals a strong spin asymmetry around the Fermi level (Figure 9). A low but finite density of states is present in the vicinity of EF, indicating the absence of a fully opened electronic gap within the ground-state DFT+U description. The valence region is dominated mainly by O 2p states, whereas Cr 3d states provide significant contributions in the unoccupied-state region above the Fermi level. The observed asymmetry between spin-up and spin-down channels confirms the spin-polarized character of the electronic structure arising from the partially filled Cr 3d orbitals.

Accepted Manuscript

ACCEPTED MANUSCRIPT

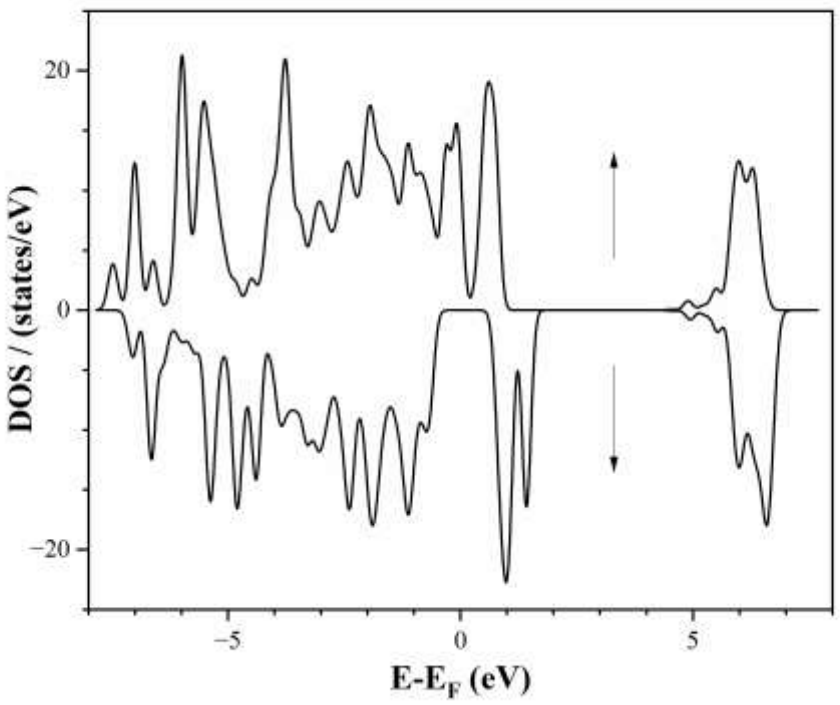


Figure 9. Density of State (DOS) of the $Ca_4Al_6CrO_{16}$

The spin-polarized projected density of states (PDOS) of $Ca_4Al_6CrO_{16}$ calculated within the PBE+U framework is shown in Fig. 10. In the PDOS plot, the contributions of Ca, Al, Cr, and O are represented by black, red, green, and blue curves, respectively. Consistent with the total DOS analysis, the electronic states in the vicinity of the Fermi level contain contributions from both O 2p and Cr 3d orbitals, indicating Cr–O orbital interactions. The occupied states below the Fermi level are mainly composed of O 2p states with noticeable mixing from Cr 3d states, while the unoccupied states above the Fermi level are primarily governed by Cr 3d orbitals. In contrast, Ca and Al contributions are mostly located far from the band edges, indicating their limited direct role in the optical transitions and confirming that chromium acts as the principal chromophore in the

ACCEPTED MANUSCRIPT

Ca–Al–Cr oxide lattice.

A clear asymmetry between the spin-up and spin-down channels is observed in the Cr-derived states, demonstrating the spin-polarized character of the electronic structure and confirming that the magnetic and electronic features of the system originate mainly from the partially filled Cr 3d orbitals. The overlap between O 2p and Cr 3d states near the valence band maximum suggests p–d hybridization between Cr and O orbitals, which is commonly associated with charge-transfer–type electronic transitions that give rise to the characteristic yellow appearance of Cr-based pigments.

The PDOS analysis clearly demonstrates that the electronic states near the Fermi level originate predominantly from hybridized Cr 3d and O 2p orbitals. The p–d hybridization identified near the band edges indicates that Cr–O interactions play an important role in determining the electronic and optical behavior of $Ca_4Al_6CrO_{16}$. These results suggest that hybridized Cr-O states are likely involved in the electronic transitions associated with the experimentally observed optical behavior of the pigment.

The observed spin asymmetry is mainly associated with the Cr 3d states, confirming that chromium is responsible for both the magnetic ordering and the spin-dependent electronic structure of $Ca_4Al_6CrO_{16}$.

Accepted Manuscript

ACCEPTED MANUSCRIPT

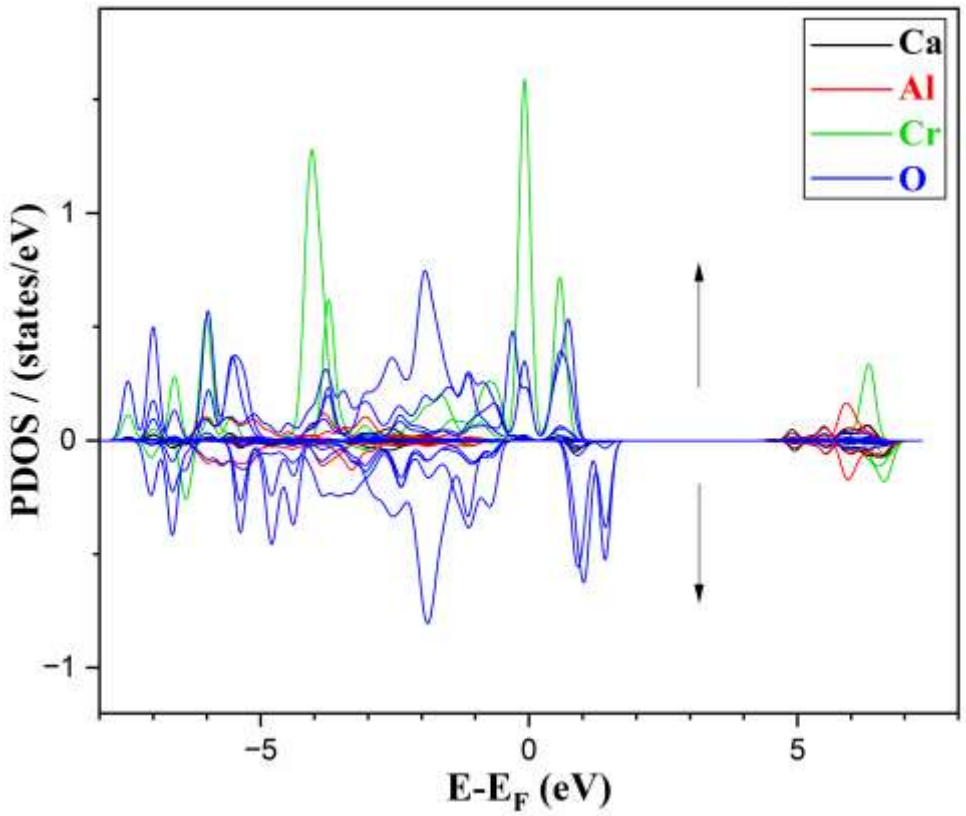


Figure 10. Projected Density of State (PDOS) of the $Ca_4Al_6CrO_{16}$ structure.

The calculated charge-density distribution and electron localization function (ELF) of $Ca_4Al_6CrO_{16}$ are presented in Figure 11. The contour maps were constructed on the crystallographic plane with Miller indices (101) and an interplanar spacing of d = 3.92379 Å in order to visualize the bonding characteristics within the lattice.

The charge-density maps clearly reveal that the electron density is strongly concentrated around the oxygen atoms, while comparatively lower charge density is observed around Ca and Al atoms. This behavior is consistent with the large electronegativity difference between oxygen and the cations, indicating a pronounced charge transfer from Ca, Al, and Cr atoms toward oxygen. Such a distribution confirms that the Ca-O and Al-O interactions are predominantly ionic in nature.

ACCEPTED MANUSCRIPT

In contrast, the charge-density contours around Cr-O bonds show noticeable electron sharing between Cr and O atoms, indicating a partial covalent character. This mixed ionic–covalent bonding is typical for transition-metal oxides and plays a key role in determining their optical and electronic properties. The presence of this partial covalency supports the formation of Cr-O hybridized states previously identified in the DOS and PDOS analyses.

The electron localization function further clarifies the bonding nature in the system. High ELF values are strongly localized around oxygen atoms, corresponding to the presence of lone-pair electrons. In contrast, Ca and Al atoms exhibit very low ELF values, confirming their largely ionic role within the lattice. Chromium atoms show intermediate ELF values, indicating partial electron localization associated with the Cr 3d orbitals. This behavior is characteristic of transition-metal chromophores and reflects the presence of localized d electrons responsible for the spin-polarized electronic structure.

The combined charge-density and ELF results demonstrate that the electronic structure of $Ca_4Al_6CrO_{16}$ is governed by significant charge transfer toward oxygen and by pronounced Cr-O hybridization. These features are consistent with charge-transfer–type electronic transitions between O 2p and Cr 3d states, which are responsible for the optical absorption in the visible region and ultimately for the yellow coloration of the pigment.

Accepted Manuscript

ACCEPTED MANUSCRIPT

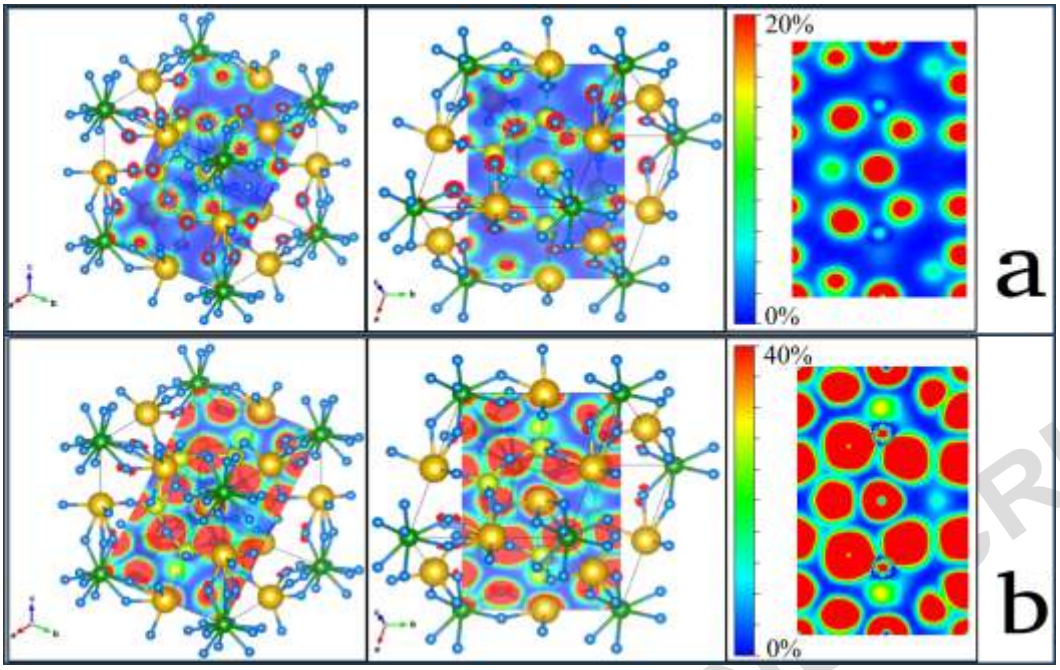


Figure 11. Visualization of (a) charge-density and (b) electron localization function (ELF) for $Ca_4Al_6CrO_{16}$, showing the spatial distribution of charge and the degree of electron localization corresponding to the bonding regions.

Although the present DFT+U calculations provided valuable insight into the electronic structure, orbital hybridization, and bonding characteristics of $Ca_4Al_6CrO_{16}$, some advanced excited-state calculations could not be completed because of computational limitations. In particular, Bethe–Salpeter Equation (BSE) calculations, which were initially considered for the simulation of optical spectra and direct comparison with experimental optical measurements, required computational resources beyond those available in the present work. Consequently, the theoretical analysis was limited to ground-state electronic properties within the DFT+U framework. Future studies employing large-scale BSE calculations may provide a more rigorous description of the optical response and color-related excitation processes in $Ca_4Al_6CrO_{16}$.

ACCEPTED MANUSCRIPT

3.3. Optical properties

3.3.1. Pigments UV-Vis spectral characterization

The UV–Vis diffuse reflectance spectrum of the synthesized LY_1 pigment in the visible wavelength range (390-740 nm) is shown in Figure 12. The spectrum exhibits a pronounced rise in reflectance from approximately 400 to 520 nm, accompanied by strong attenuation in the violet–blue region. This response is typical of yellow pigments and is consistent with the complementary relationship between yellow and blue–violet wavelengths. A distinct reflectance minimum occurs near 400 nm, corresponding to the characteristic absorption band associated with yellow coloration [49, 50]. At longer wavelengths, the reflectance reaches a maximum near 580 nm within the green–yellow region, consistent with the intense yellow appearance of LY_1.

The optical energy gap of the pigment was estimated by applying the Tauc plot to the UV–Vis diffuse-reflectance data, as shown in Figure 12, with the corresponding values summarized in Table 7. The LY_1 sample exhibits an optical band gap of approximately 2.91 eV. This value is consistent with electronic transitions associated with hexavalent chromium (Cr^{6+}) ions situated in distorted octahedral coordination environments, which are characteristic of $Ca_4Al_6CrO_{16}$-type crystal structures [22, 25].

Accepted Manuscript

ACCEPTED MANUSCRIPT

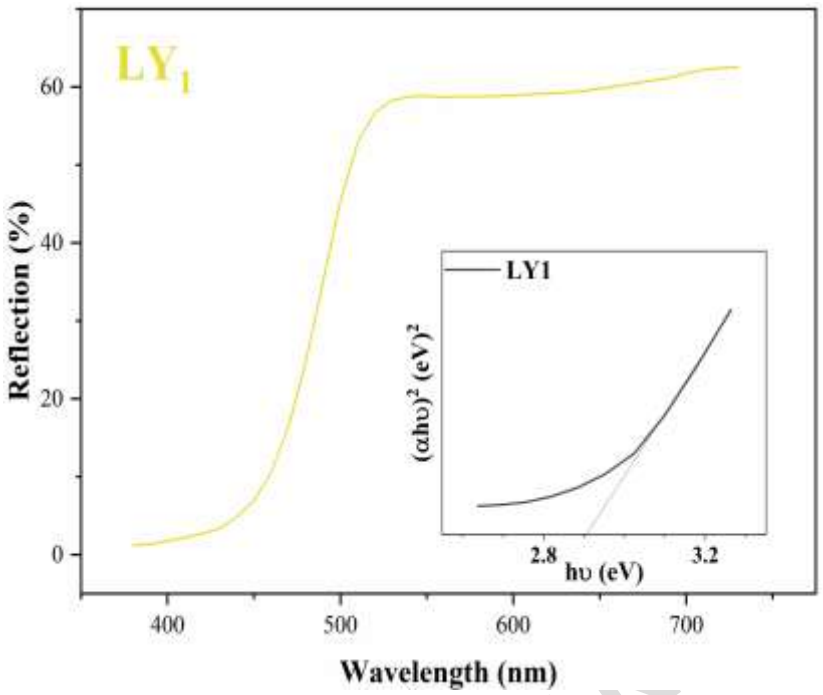


Figure 12. UV-Vis reflectance spectrum for LY_1.

Comparable spectral characteristics were obtained for the remaining pigments, as shown in Figure 13. In each case, the reflectance increases steeply within the 400-520 nm interval, while a pronounced minimum is retained around 400 nm and a maximum occurs close to 580 nm. These features confirm that the synthesized compositions exhibit the characteristic optical response of yellow inorganic pigments [49, 50].

Among the investigated pigments, LY_6 exhibits the highest reflectance across the visible region (approaching ~90%), indicating a highly bright yellow appearance. LY_4 and LY_3 also show relatively high and nearly flat reflectance curves, suggesting comparable brightness and good color purity. In contrast, LY_2 presents the lowest reflectance over the visible range, particularly between 480 and 700 nm, reaching a maximum reflectance of only about 50%, indicating a darker and less saturated yellow shade. This response is comparable to that of LY_1, and the lower brightness of both

ACCEPTED MANUSCRIPT

compositions can be associated with their nearly single-phase character and the absence of $CaAl_2O_4$.

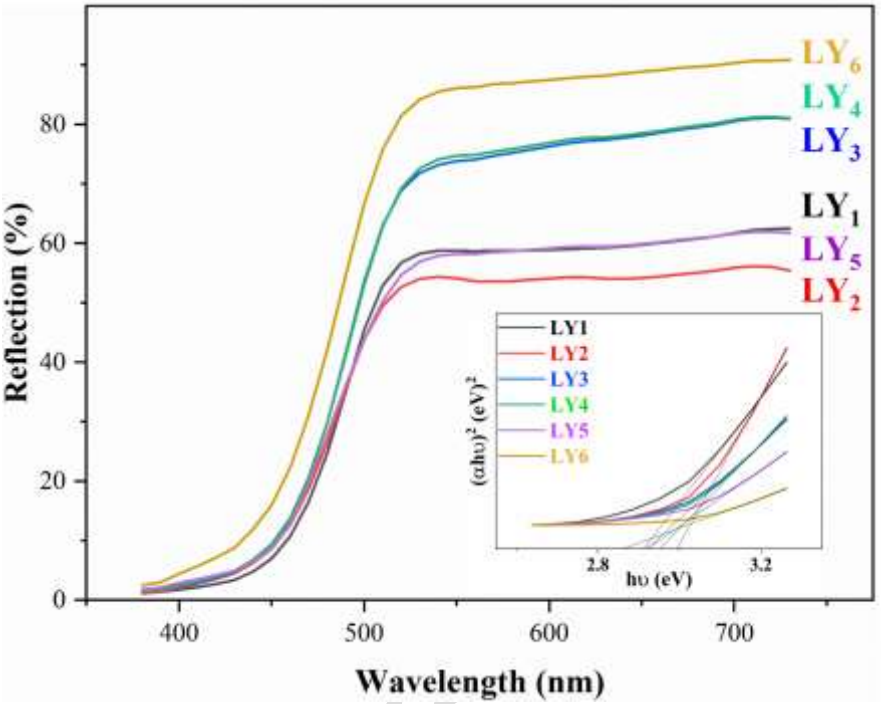


Figure 13. UV-Vis diffuse reflectance spectra of pigments LY_1– LY_6.

3.3.2. Pigments CIELAB color measurement

The CIELAB measurements obtained for LY_1–LY_6 are summarized in Table 8 and presented in Figure 14. The measured b* coordinates are positive and exceed 54, confirming their yellow coloration, while all samples show negative a* coordinates, indicative of a slight greenish component commonly observed in chromium-containing yellow pigments. This greenish contribution is more pronounced for the nearly single-phase LY_1 and LY_2 compositions, whereas LY_3-LY_6 exhibit a comparatively purer yellow appearance.

Among the investigated compositions, LY_4 provides the most pronounced yellow response, with b* = 67.4, together with a high L* value of 87.7, corresponding to high

ACCEPTED MANUSCRIPT

brightness and color purity. Notably, the yellowness obtained in the present work is considerably higher than that measured for the pigments investigated in our previous study [6].

The synthesized $Ca_4Al_6CrO_{16}$ compositions demonstrated color strengths that were comparable to or greater than those of established commercial yellow pigments, including zircon–praseodymium and nickel–antimony–titanium yellow systems (CPMA 14-43-4 and 11-15-4, respectively) [44, 45, 54]. The highest chromatic response was obtained for LY_4 (b* = 67.4; C* = 67.9), together with high resistance to thermal and chemical degradation. For the pigments prepared at 1200 °C, variations in particle size are accompanied by corresponding changes in both reflectance and the CIELAB parameters. In general, reduction in particle size is associated with higher overall reflectance together with increased b* and L* values, indicating stronger yellowness and greater brightness (Tables 2, 3 and 8). This behavior suggests that differences in particle size and other microstructural characteristics may contribute to the observed variations in optical response.

LY_4 represents the most favorable combination within this series, exhibiting the smallest average particle size (630 nm; median: 633 nm), the highest color saturation, and the highest brightness. The resulting vivid yellow appearance is consistent with enhanced light-scattering efficiency associated with smaller particles, which may arise from the increased surface-to-volume ratio and more uniform pigment dispersion [55].

A discernible pattern emerges throughout the pigments synthesized at 1200°C, especially when examining variations in the $CaCO_3$:Al_2O_3 molar ratios. Collectively, the findings underscore the pivotal role of the Ca:Al:Cr molar ratio in modulating the optical

ACCEPTED MANUSCRIPT

characteristics of these Cr-doped pigments [6]. Although in our previous work an increase in $CaCO_3$ content led to higher b* values and stronger yellow coloration, the present study reveals an almost opposite tendency, where decreasing $CaCO_3$ content results in higher b* values and more intense yellow color.

In this study, the compositional design was initiated from the single-phase $Ca_4Al_6CrO_{16}$ composition and then extended toward nearby stoichiometries where the amount of secondary phases remains minimal. In contrast, the earlier work contained a considerably higher fraction of secondary phases. These observations suggest that an optimal composition likely exists between these two compositional ranges; where maximum yellowness and b* values can be achieved. The current compositions appear close to this optimum, since all samples remain near the single-phase $Ca_4Al_6CrO_{16}$ region with limited secondary phases and exhibit significantly higher yellowness and b* values compared with our previous study. Identifying this optimum composition more precisely will be the focus of future research.

The band gap energies obtained from the UV-Vis diffuse reflectance data using the Tauc approach are presented in Figure 13 and listed in Table 7. All pigments display optical band gap values in the range of 2.86-2.99 eV, which can be attributed to electronic transitions of Cr^{6+} ions located in distorted octahedral coordination environments characteristic of $Ca_4Al_6CrO_{16}$-type crystal structures [22, 25].

Accepted Manuscript

ACCEPTED MANUSCRIPT

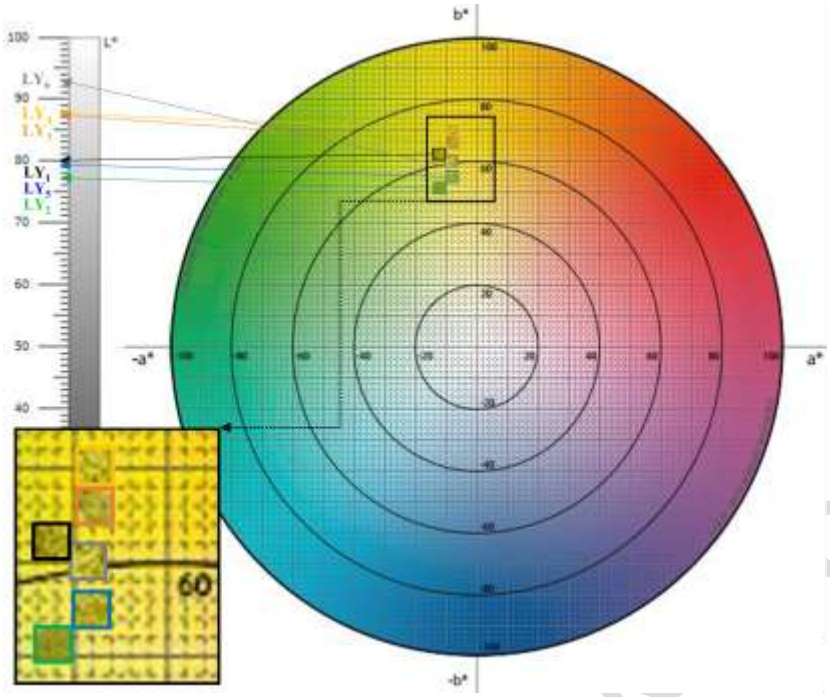


Figure 14. CIELAB colorimetric coordinates illustrating the color positions of pigments LY_1-LY_6.

A similar trend is also evident between particle size and band gap for the pigments synthesized at 1200 °C. As the particle size decreases, a slight increase in the band gap is observed. In other words, pigments synthesized at 1200 °C exhibit higher yellowness (b*), chroma (C*), and lightness (L*) and also tend to show larger band gap values (Figure 15).

ACCEPTED MANUSCRIPT

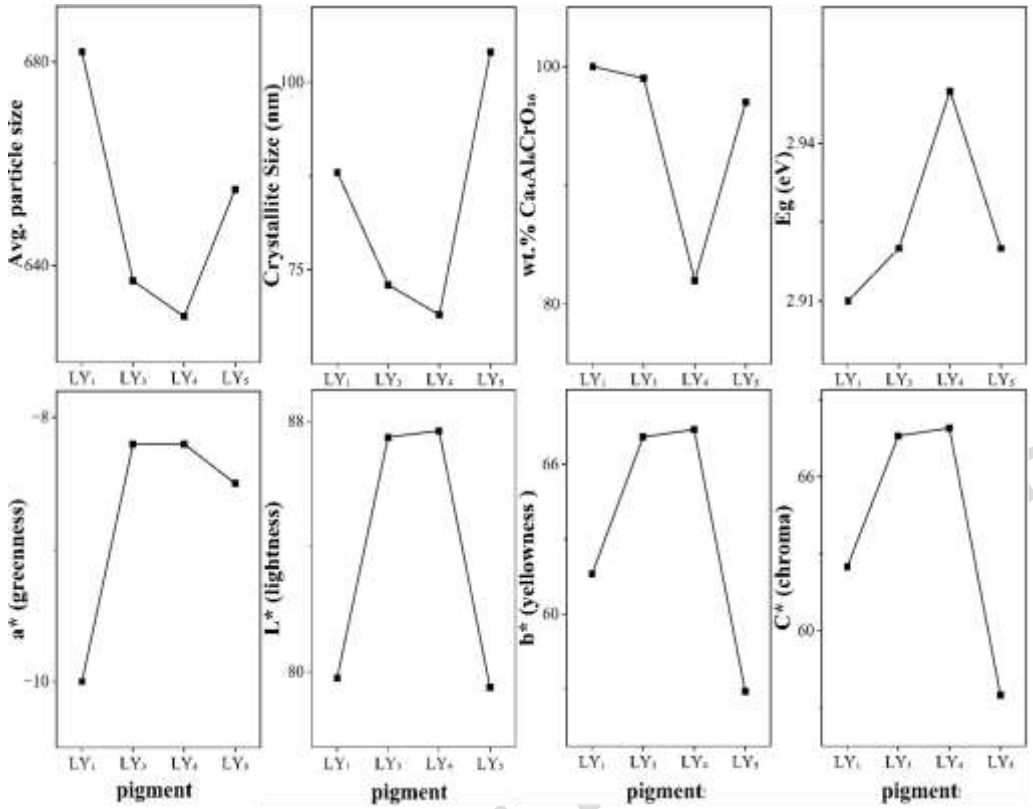


Figure 15. A clear correlation is observed for pigments synthesized at 1200 °C: decreasing average particle size is accompanied by reductions in crystallite size, $Ca_4Al_6CrO_{16}$ mass fraction, and greenness (|a*|), along with increases in band gap, lightness (L*), yellowness (b*) and chroma (C*).

This modest band gap widening can be attributed to variations in crystallite size, which can subtly alter the electronic environment at the atomic scale and influence the energetic states associated with Cr-based chromophore centers. These observations indicate that the measured optical gap is governed by a combination of compositional and phase characteristics, together with microstructural factors such as crystallite size and synthesis temperature [56].

ACCEPTED MANUSCRIPT

3.4. PU coatings

3.4.1. PU Coatings UV-Vis spectral characterization

The UV-Vis reflectance spectra recorded for the YP_1–YP_6 polyurethane coatings over the 390–740 nm wavelength interval are presented in Figure 16. A broad low-reflectance region is observed from approximately 390 to 480 nm, followed by a marked increase toward 600 nm, where the reflectance reaches its maximum in the yellow–red portion of the spectrum. This spectral profile is consistent with preferential attenuation of violet–blue wavelengths and enhanced reflection at longer visible wavelengths, which accounts for the characteristic yellow appearance of the pigmented coatings. The resulting spectral balance contributes to the brightness and chromatic saturation perceived in the polymer films.

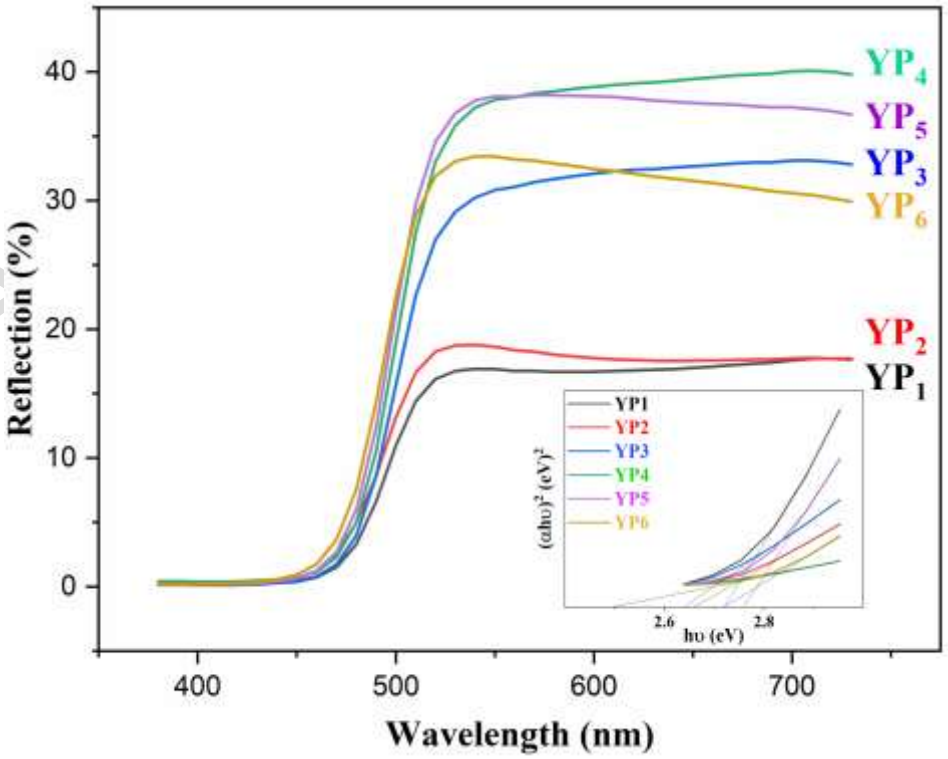


Figure 16. UV-Vis diffuse reflectance spectra of pigmented polymer coatings.

ACCEPTED MANUSCRIPT

The estimated optical band gaps, obtained from the UV–Vis diffuse-reflectance data of the YP_1-YP_6 coatings using the Tauc method, ranged from 2.50 to 2.76 eV (Figure 16 and Table 7). YP_5 possesses the largest estimated value (2.76 eV), whereas YP_4 exhibits the smallest (2.50 eV).

Unlike the trends identified for the corresponding samples calcined at 1200 °C, the sequence of band-gap values in the polyurethane coatings varies in the opposite direction. Thus, a band-gap increase observed between two pigment compositions is generally accompanied by a decrease in the corresponding coated samples, and vice versa. This behavior can be related to the fact that the measured optical response of the composite coating is not determined solely by the intrinsic electronic structure of the inorganic phase. Instead, particle dispersion within the polyurethane, pigment–binder interfacial interactions, and the combined effects of scattering and absorption in the composite layer can substantially modify the apparent optical response. For the powder pigments, the band-gap variation is primarily associated with crystallite size and intrinsic electronic characteristics, whereas the polymer environment introduces additional interfacial and microstructural factors. Improved pigment dispersion and stronger interfacial interactions may enhance electronic coupling within the composite and thereby reduce the effective optical band gap, while less homogeneous dispersion and stronger scattering can produce the opposite response. These observations demonstrate that the optical behavior of the pigmented polyurethane coatings arises from the combined contribution of the pigment itself and its surrounding polymer environment.

Accepted Manuscript

ACCEPTED MANUSCRIPT

3.4.2. PU coatings CIELAB color measurement

The CIELAB response of the YP_1-YP_6 coatings is summarized by the color coordinates obtained for each formulation. YP_1 and YP_2 display lower b* values than the other pigmented polymer coatings (54.0 and 51.6, respectively). Although these b* values are not small, their negative a* values combined with the lowest L* values result in a perceptible greenish appearance. By contrast, YP_3–YP_6 exhibit markedly positive b* values of 65.5–75.9, confirming a pronounced yellow character. Among them, YP_4 presents the highest b* value (75.9), reflecting the strongest yellow hue, with YP_5 and YP_3 ranking next in intensity. YP_4 and YP_5 also show the highest L* value (65.9), whereas YP_6 and YP_3 exhibit lower values of 62.6 and 60.6, respectively. All samples show a slight displacement toward negative a* values, consistent with a weak green component characteristic of chromium-containing yellow pigments. For YP_4, the comparatively less negative a* value, together with its exceptionally high b* value, corresponds to the weakest greenish tendency and the most pronounced yellow response among the investigated coatings.

A clear distinction is observed between the nearly single-phase LY_1-LY_2 compositions and the $Ca_4Al_6CrO_{16}$/$CaAl_2O_4$-containing LY_3-LY_6 compositions. Both as powders and after incorporation into PU, the single-phase compositions exhibit a slightly greenish-yellow hue [23], whereas the presence of $CaAl_2O_4$ in LY_3–LY_6 is associated with a purer yellow appearance and higher yellowness and brightness [6].

The effect of the PU matrix on the colorimetric parameters differs according to phase composition. For the single-phase compositions, the incorporation into PU leads to decreases in L*, a*, b*, and C* relative to the corresponding pigments. In contrast, the

ACCEPTED MANUSCRIPT

two-phase yellow compositions generally exhibit higher b* values after incorporation into the polymer, indicating an appreciable enhancement in yellowness. The increase is particularly notable for YP_5, for which b* rises from 56.9 to 74.2. YP_4 shows the most pronounced yellow response overall, increasing from b* = 67.4 for the pigment to 75.9 for the corresponding coating. After coating, the a* values become less negative, indicating a reduction in the greenish component and a shift toward a purer yellow tone. At the same time, L* values decrease in the coating state relative to the pigment powders.

Such a reduction in brightness and reflectance when transitioning from pigment powders to polymer coatings is commonly reported [57], since pigments embedded in a polymer matrix experience lower light scattering efficiency due to refractive-index matching, partial light absorption by the binder, and reduced multiple scattering compared with loose powder layers. These effects typically lead to a decrease in measured reflectance and L* values in coated systems.

The enhanced b* and chroma values observed for the two-phase coatings may be related to several concurrent effects, including pigment–polymer interactions, improved dispersion of pigment particles, and changes in light scattering caused by the microstructure of the cured coating [20, 57].

In terms of hue angle parameter (h°), the samples were located around 97-100°, placing them in the yellow–green color range. After coating, the hue values decreased slightly to 94-98°, indicating a subtle movement toward a purer, brighter yellow tone with reduced greenish character.

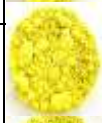
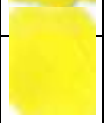
Accepted Manuscript

ACCEPTED MANUSCRIPT

Table 7. Optical band gaps for pigments and their polymer coatings.

Pigments	Eg (eV)	Polymers	Eg (eV)
LY_1	2.91	YP_1	2.72
LY_2	2.99	YP_2	2.66
LY_3	2.92	YP_3	2.64
LY_4	2.95	YP_4	2.50
LY_5	2.92	YP_5	2.76
LY_6	2.86	YP_6	2.72

Table 8. CIELAB colorimetric parameters for pigments and pigmented PU coatings.

Sample	Type	L*	a*	b*	C*	h°	Image	Sample	Type	L*	a*	b*	C*	h°	Image
LY_1	Pigment	79.8	-10	61.6	62.5	100		**YP_1**	Polymer	46.8	-7.2	54.0	54.4	98	
LY_2	Pigment	77.3	-10	54.2	55.2	101		**YP_2**	Polymer	48.7	-9.5	51.6	52.5	100	
LY_3	Pigment	87.5	-8.2	67.1	67.6	97		**YP_3**	Polymer	60.6	-4.7	71.9	72.1	94	
LY_4	Pigment	87.7	-8.2	67.4	67.9	97		**YP_4**	Polymer	65.9	-5.5	75.9	76.1	94	
LY_5	Pigment	79.5	-8.5	56.9	57.5	99		**YP_5**	Polymer	65.9	-8.1	74.2	74.6	96	
LY_6	Pigment	93.0	-9.5	61.3	62.0	99		**YP_6**	Polymer	62.6	-10	65.5	66.3	99	

3.4.3. PU coatings microstructure

To assess the morphology and particle-size characteristics of the pigments before incorporation into polyurethane, SEM observations were carried out for LY_1-LY_6. In the coated state, SEM analysis was focused on YP_1 and YP_4. Sample YP_1, derived from single-phase $Ca_4Al_6CrO_{16}$, was selected as a reference to represent the baseline microstructure of the pure pigment within the matrix. Sample YP_4 was chosen because it exhibited the best overall colorimetric and optical performance. Accordingly, these two formulations were selected as representative systems for evaluating the microstructure of

ACCEPTED MANUSCRIPT

the cured polymer layer and its relationship with pigment characteristics. Figure 17 presents the surface morphology and particle-size distributions obtained for YP_1 and YP_4. The embedded pigment particles exhibit predominantly irregular morphologies, with plate-like and angular features, while some particles show approximately elliptical outlines.

Some agglomeration is visible in the micrographs, which may be related to the relatively long interval between coating preparation and SEM observation, as well as possible particle adhesion and partial sintering during processing. Nevertheless, the measured particle dimensions provide a representative description of the dispersion state because the principal pigment morphology remains discernible. The mean particle dimension, together with the maximum and minimum values, is summarized in Table 9. The mean particle sizes were 386 nm for YP_1 and 384 nm for YP_4, compared with 682 and 630 nm, respectively, for the corresponding pigment powders. This reduction indicates that the dispersion and mixing processes during coating preparation partially broke down a substantial fraction of the initial agglomerates. Although several larger particles are still present, the majority of the particles remain within the submicron range (<600 nm), indicating that the fine particle structure is largely preserved even after prolonged storage.

Relative to YP_1, YP_4 exhibits a more uniform surface coverage, with fewer pigment-free regions and a more continuous spatial distribution of particles throughout the polymer layer. This difference in surface microstructure may contribute to the superior optical and colorimetric response of YP_4 observed in the CIELAB measurements.

Accepted Manuscript

ACCEPTED MANUSCRIPT

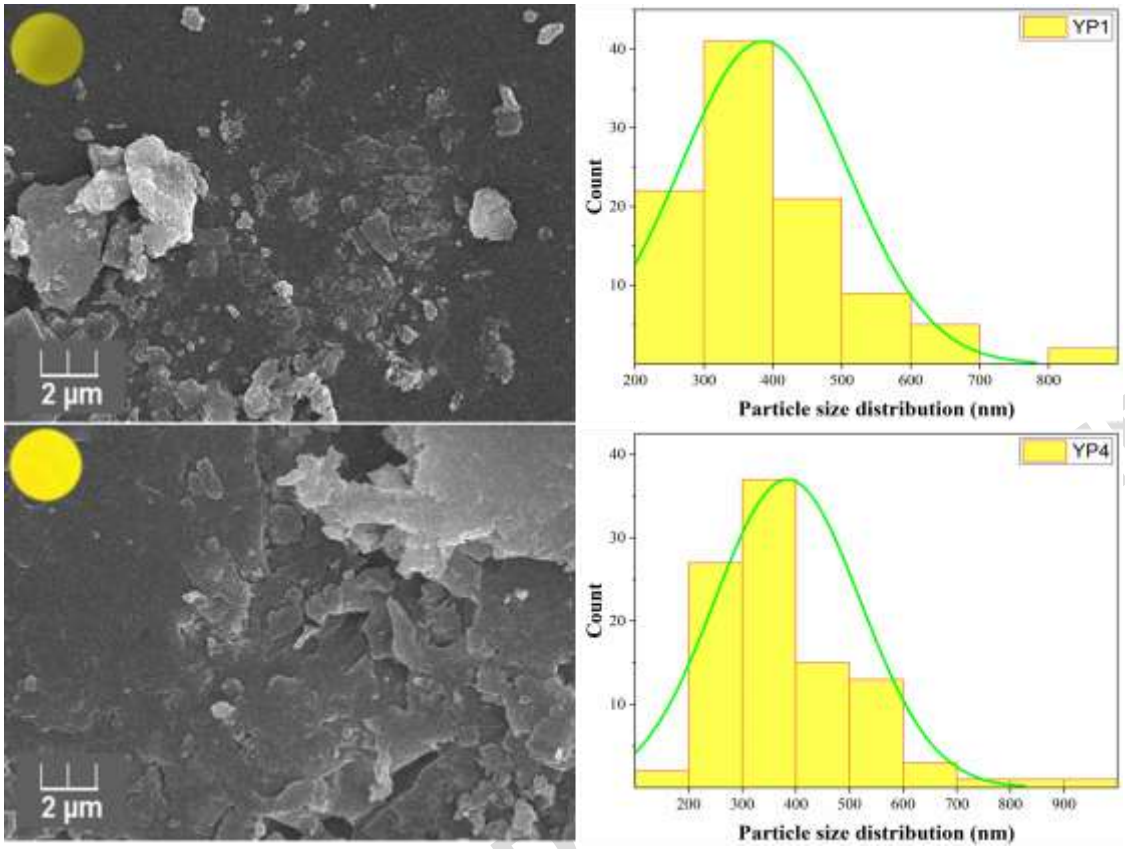


Figure 17. SEM images and particle size histograms of polymer coatings containing YP_1 and YP_4.

Table 9. Particle size data of the pigmented polymer coatings derived from YP_1 and YP_4.

sample	Minimum particle size (nm)	Maximum particle size (nm)	Average particle size (nm)
YP_1	218	841	386
YP_4	191	929	384

4. Conclusion

The experimental results demonstrate that $Ca_4Al_6CrO_{16}$-based Ca–Al–Cr oxides can provide yellow pigments with composition-dependent structural and optical characteristics. Under the selected preparation conditions, LY_1 and LY_2 exhibited single-

ACCEPTED MANUSCRIPT

phase $Ca_4Al_6CrO_{16}$, whereas LY_3–LY_6 contained $CaAl_2O_4$ as a secondary phase. XRD and Rietveld refinement confirmed the corresponding phase compositions and crystallographic parameters. Among the pigments calcined at 1200 °C, LY_4 exhibited the smallest average particle size (630 nm; median: 633 nm), the highest b* value (67.4), and the lowest greenness, indicating the highest yellow purity.

For the 1200 °C series, changes in precursor composition affected the $Ca_4Al_6CrO_{16}$ phase fraction, particle size, and colorimetric properties. LY_4 provided particularly favorable color performance, while maintaining the high chemical and thermal stability associated with the $Ca_4Al_6CrO_{16}$-based system. After incorporation into polyurethane, the characteristic yellow coloration was retained and enhanced. The corresponding YP_4 coating exhibited the highest yellowness, with b* increasing from 67.4 for LY_4 to 75.9.

First-principles DFT+U calculations performed for LY_1 provided insight into the electronic and magnetic characteristics of $Ca_4Al_6CrO_{16}$. The electronic structure was dominated by O 2p and Cr 3d states, with pronounced Cr–O orbital interactions and spin-dependent electronic behavior. The calculations also yielded a cohesive energy of −5.64 eV $atom^{-1}$ and a total magnetization of 8.00 μB/cell, providing further insight into the structural stability and magnetic characteristics of the phase.

Taken together, the results demonstrate that precursor composition and calcination conditions can regulate phase formation, particle morphology, and color performance of $Ca_4Al_6CrO_{16}$-based pigments. The combined experimental and theoretical results establish structure–property relationships and demonstrate the potential of these pigments for polyurethane coloration. Further optimization of composition and polymer–pigment interactions may provide additional improvements in chromatic performance and

Accepted Manuscript

ACCEPTED MANUSCRIPT

application properties.

Acknowledgement

The authors gratefully acknowledge Yazd University for its financial support and for providing access to the Nano Pigments and Coatings Laboratory within the Department of Physics. The authors also thank Dr. Reza Dehghan Banadaki for his assistance with reflectance-spectrum measurements.

5. References

1. Barna E. Synthesis and characterization of scratch resistant polyurethane clear coatings by incorporation of surface modified nanoparticles. University of Basel, Zurich. 2010. https://doi.org/10.1016/j.porgcoat.2016.11.022

2. Mirabedini S, Sabzi M, Zohuriaan-Mehr J, Atai M, Behzadnasab M. Weathering performance of the polyurethane nanocomposite coatings containing silane treated TiO_2 nanoparticles. Appl Surf Sci. 2011; 257(9):4196–203. https://doi.org/10.1016/j.apsusc.2010.12.020

3. Zhan F, Xiong L, Liu F, Li C. Grafting hyperbranched polymers onto TiO_2 nanoparticles via thiol-yne click chemistry and its effect on the mechanical, thermal and surface properties of polyurethane coating. Mater. 2019;12(17):2817. https://doi.org/10.3390/ma12172817

4. Jose S, Joshy D, Narendranath SB, Periyat P. Recent advances in infrared reflective inorganic pigments. Sol Energy Mater Solar Cell. 2019; 194:7-27. https://doi.org/10.1016/j.solmat.2019.01.037

ACCEPTED MANUSCRIPT

5. Zhou X, Hao Y, He X, Zhou D, Xie L, Liu S, et al. Protean morphology of waterborne polyurethane dispersion: an overview of nanoparticles from sphere to irregular elongated shape. Prog Org Coat. 2020; 146:105742. https://doi.org/10.1016/j.porgcoat.2020.105742

6. Jalili M, Aminian MK, Shahsavari F. Synthesis and study the physical properties of calcium aluminate compound doped by chromium atoms as a yellow ceramic pigment. Ceram Internat. 2025. https://doi.org/10.1016/j.ceramint.2025.11.390

7. Elakkiya V, Sumathi S. Low-temperature synthesis of environment-friendly cool yellow pigment: Ce substituted $SrMoO_4$. Mater Lett. 2020; 263:127246. https://doi.org/10.1016/j.matlet.2019.127246

8. Elakkiya V, Sumathi S. Ce and Fe doped gahnite: Cost effective solar reflective pigment for cool coating applications. J Alloy Compound. 2020; 820:153174. https://doi.org/10.1016/j.jallcom.2019.153174

9. Monrós G, Llusar M, Badenes JA. Eco-friendly polyfunctional ceramic pigments: an approach. Pigm Resin Technol. 2024; 53(6):716-29. https://doi.org/10.1108/prt-04-2022-0038

10. Lavat AE, Gayo GX. New Environmental friendly yellow ceramic pigments of the type (FeIIIMV)-TiO_2. 2014.

11. Rafiq R, Aminian MK, Vaselnia S, Banadaki RD. Structural, electronic, and optical properties of $CaCoSi_2O_6$ and $Ca_2CoSi_2O_7$ blue pigments: a combined experimental, dft+ u, and bse study. J Solid State Chem. 2024; 330:124463. https://doi.org/10.1016/j.jssc.2023.124463

Accepted Manuscript

ACCEPTED MANUSCRIPT

12. Hu Z, Wang Q, Liu J, Liu K, Zhang W, Yang Y, et al. Synthesis and chromatic properties of V-doped and V/Y-codoped ZrO_2 yellow pigments. J Alloys Compound. 2021; 856:157397. https://doi.org/10.1016/j.jallcom.2020.157397

13. Chen J, Li Y, Feng G, Jiang F, Zhao Q, Lan S, et al. Novel yellow to blackish green Ni-doped aluminium titanate ceramic pigments. Process Appl Ceram. 2021; 15(3):314-318. https://doi.org/10.2298/pac2103314c

14. Zhou X, Zhang X, Zou C, Chen R, Cheng L, Han B, et al. Insight into the effect of counterions on the chromatic properties of Cr-doped rutile TiO_2-based pigments. Materials. 2022; 15(6):2049. https://doi.org/10.3390/ma15062049

15. Buxbaum G. Industrial inorganic pigments: John Wiley & Sons; 2008.

16. Feldmann C. Preparation of nanoscale pigment particles. Adv Mater. 2001;13(17):1301-3. https://doi.org/10.1002/1521-4095(200109)13:17.

17. Ocana M. Nanosized Cr_2O_3 hydrate spherical particles prepared by the urea method. J Europ Ceram Soc. 2001; 21(7):931-9. https://doi.org/10.1016/s0955-2219(00)00288-0

18. Rangappa D, Naka T, Kondo A, Ishii M, Kobayashi T, Adschiri T. Transparent $CoAl_2O_4$ hybrid nano pigment by organic ligand-assisted supercritical water. J Am Chem Soc. 2007; 129(36):11061-6. https://doi.org/10.1021/ja0711009

19. Galindo Llorach R, Gargori C, Fas N, Llusar M, Monrós G. New chromium doped powellite (Cr–$CaMoO_4$) yellow ceramic pigment. Ceram Inter. 2015; 41(5):6364-6372. https://doi.org/10.1016/j.ceramint.2015.01.071

ACCEPTED MANUSCRIPT

ACCEPTED MANUSCRIPT

20. Enríquez E, Reinosa J, Fuertes V, Fernández J. Advances and challenges of ceramic pigments for inkjet printing. Ceram Inter. 2022; 48(21):31080-101. https://doi.org/10.1016/j.ceramint.2022.07.155

21. Xu T, Xu Y, Li Y, Nath M. Inhibition of Cr (VI) in the Al_2O_3-CaO-Cr_2O_3 castables by using $(Al1-x,Crx)_2O_3$ solid solution. 2020. https://doi.org/10.21203/rs.3.rs-123797/v1

22. Liu D, Song S, Garbers-Craig AM, Xue Z, Nath M, Ma G, et al. High-temperature stability and leaching kinetics of the hexavalent chromium compound, chrome-hauyne ($Ca_4Al_6CrO_{16}$). Ceram Inter. 2021; 47(I24):34012-9. https://doi.org/10.1016/j.ceramint.2021.08.309

23. Zhang J, Lu C. Study on the product 3 $CaO_3Al_2O_3$. $CaCrO_4$ in the reaction between magnesite-chrome refractory brick and cement clinker. J Chin Ceram Soc. 1990; 18(1):83-90.

24. Wu Y, Song S, Xue Z, Nath M. Effect of temperature on hexavalent chromium formation in $(Al, Cr)_2O_3$ with calcium aluminate cement in air. ISIJ International. 2019; 59(7):1178-83. https://doi.org/10.2355/isijinternational.isijint-2018-699

25. Xu T, Xu Y, Liao N, Li Y, Nath M. High-temperature chemical stability of Cr (III) oxide refractories in the presence of calcium aluminate cement. Materials. 2021; 14(21):6590. https://doi.org/10.3390/ma14216590

26. Eliopoulos I-PD, Eliopoulos GD, Economou-Eliopoulos M. The cr (Vi) stability in contaminated coastal groundwater: Salinity as a driving force. Minerals. 2021; 11(2):160. https://doi.org/10.3390/min11020160

Accepted Manuscript

ACCEPTED MANUSCRIPT

27. Edition F. Guidelines for drinking-water quality. WHO chronicle. 2011; 38(4):104–8.

28. EPA: Washington DC, USA. Toxicological review of hexavalent chromium. 1998. https://nepisepagov/Exe/ZyPURLcgi?Dockey=P1006B2Ztxt..

29. Mizuhara Shigeharu UT, Yamaguchi Akiyoshi, Maeda Tomoyuki, editor Leaching of hexavalent chromium compounds produced by the use of chromium-based refractories. Proceedings of the 22nd Annual Meeting of the Japan Society of Material Cycles and Waste Management; 2011: Japan Society of Waste Management.

30. Vaselnia S, Khajeh Aminian M. Review on the application of density functional theory to predict the color, electronic, and optical properties of ceramic pigments along with experimental confirmation. J Mater Sci. 2024; 1-37. https://doi.org/10.1007/s10853-024-10455-4

31. Vaselnia S, Aminian MK, Motahari H. Fe-doped titanite pigment: Synthesis, DFT/TDDFT calculations by Lanczos and Bethe-Salpeter equation methods and comparison of computational and experimental color properties. J Phys Chem Solids. 2020; 138:109244. https://doi.org/10.1016/j.jpcs.2019.109244

32. Vaselnia S, Aminian MK, Banadaki RD. Experimental and theoretical study on the structural, electronic, and optical properties within DFT+ U, Fxc kernel for LRC model, and BSE approaches. Part I: $CoTiO_3$ and Co_2TiO_4 pigments. Powder Technol. 2021; 390:50-61. https://doi.org/10.1016/j.powtec.2021.05.070

33. Dehghan Banadaki R, Khajeh Aminian M, Vaselnia S. Study the effect of doping cobalt ions into Zn (2−x) Co_xSiO_4 [x= 0, 0.056 and 0.167] structures on the optical

ACCEPTED MANUSCRIPT

properties and color parameters: experiment and calculation. Appl Phys A. 2024; 130(3):162: 1-16. https://doi.org/10.1007/s00339-024-07309-w

34. Vaselnia S, Aminian MK, Motahari H, Banadaki RD. A joint experimental and theoretical study on the structural, electronic and optical properties of malayaite and Chromium-doped malayaite structures as pigments. J Phys Chem Solid. 2020; 141:109402. https://doi.org/10.1016/j.jpcs.2020.109402

35. Titorenkova R, Kostov-Kytin V, Dimitrov T. Synthesis, phase composition and characterization of Co-diopside ceramic pigments. Ceram Inter. 2022; 48(24):36781-8. https://doi.org/10.1016/j.ceramint.2022.08.242

36. Espresso Q. a modular and open-source software project for quantum simulations of materials/P. Giannozzi [et al.]. J Phys: Condens Matter. 2009; 21(39):395502.

37. Giannozzi P, Andreussi O, Brumme T, Bunau O, Nardelli MB, Calandra M, et al. Advanced capabilities for materials modelling with Quantum ESPRESSO. J Phys: Cond Mater. 2017; 29(46):465901. https://doi.org/10.1088/1361-648X/aa8f79

38. Hassan I. Direct observation of phase transitions in aluminate sodalite $Ca_8[Al_{12}O_{24}](CrO_4)_2$. American Mineralogist. 1996; 81(11-12):1375-9. https://doi.org/10.2138/am-1996-11-1210

39. Antao SM, Hassan I, Parise JB. Chromate aluminate sodalite, $Ca_8[Al_{12}O_{24}](CrO_4)_2$: Phase transitions and high-temperature structural evolution of the cubic phase. Canadian Mineralogist. 2004; 42(4):1047-56. https://doi.org/10.2113/gscanmin.42.4.1047

40. Nadiyyah K, Aprianti R, Zakirman Z, Widiasih W, Jhora FU, Ratnawulan R. Enhancing student comprehension of crystal structures: The effectiveness of Vesta as a

ACCEPTED MANUSCRIPT

learning tool. Moment Phys Education J. 2025; 9(1):69-79. https://doi.org/10.21067/mpej.v9i1.10448

41. Momma K, Izumi F. VESTA 3 for three-dimensional visualization of crystal, volumetric and morphology data. Appl Crystallography. 2011; 44(6):1272-6. https://doi.org/10.1107/s0021889811038970

42. Timrov I, Marzari N, Cococcioni M. HP–A code for the calculation of Hubbard parameters using density-functional perturbation theory. Computer Phys Commun. 2022; 279:108455. https://doi.org/10.1016/j.cpc.2022.108455

43. Williamson G, Hall W. X-ray line broadening from filed aluminium and wolfram. Acta Metallurgica. 1953; 1(1):22-31. https://doi.org/10.1016/0001-6160(53)90006-6

44. Cerro S, Llusar M, Gargori C, Monrós G. Cool and photocatalytic yellow ceramic pigments; from lead-tin to Cr doped scheelite pigments. Ceram Inter. 2019; 45(4):4613-25. https://doi.org/10.1016/j.ceramint.2018.11.150

45. Monrós G, Badenes JA, Llusar M. Ecofriendly high NIR reflectance ceramic pigments based on rare earths compared with classical chromophores prepared by DPC method. Ceramics. 2022; 5(4):614-41. https://doi.org/10.3390/ceramics5040046

46. Berent K, Komarek S, Lach R, Pyda W. The effect of calcination temperature on the structure and performance of nanocrystalline mayenite powders. Materials. 2019; 12(21):3476. https://doi.org/10.3390/ma12213476

47. Dong W, Bao Q, Huang X, Gu X, Wang X, Huang Y, et al. Synthesis of new Cr-doped $CaTiO_3$ yellow pigments by a simple solvothermal method. J Ceram Soc Japan. 2017; 125(2):71-4. https://doi.org/10.2109/jcersj2.16154

ACCEPTED MANUSCRIPT

48. Yekta BE, Tamizifar M, Rahimi N. Synthesis of a zircon-cadmium sulfo selenide pigment by a sol-gel technique. J Ceram Soc Japan. 2007; 115(1347):757-60. https://doi.org/10.2109/jcersj2.115.757

49. YONGVANICH N, SOYSOM P, RATKASEMSAK W. Synthesis of zircon pigments from rice husk ash and their performance in ceramic glaze. J Metals Mater Miner. 2023; 33(1):47-55. https://doi.org/10.55713/jmmm.v33i1.1593

50. Pyon K-R, Lee B-H. The influence of firing conditions on the color properties of Pr-ZrSiO 4 pigments synthesized using rice husk ash. J Korean Ceram Soc. 2009; 46(4):397-404.

51. Saville AI, Creuziger A, Mitchell EB, Vogel SC, Benzing JT, Klemm-Toole J, et al. MAUD rietveld refinement software for neutron diffraction texture studies of single- and dual-phase materials. Integ Mater Manuf Innovation. 2021; 10(3):461-87. https://doi.org/10.1007/s40192-021-00224-5

52. Joseph EA, Haque M. The cohesive energy calculations of some bcc (li, cr, fe, mo) lattices using density functional theory. Asian J Phys Chem Sci. 2016; 1(2):1-10.

53. Abdullah BJ, Omar MS, Saadi NS, Jiang Q. First-principles calculations on cohesive energy of bulk and nano Si. Int J Sci Eng Res. 2015;6(9):842-6.

54. Fitzpatrick HF, Merritt G, Robinson JL. CPMA - Classification and Chemical Descriptions of the Complex Inorganic Color Pigments. 4th ed2010.

55. Elias M. Relationship between the size distribution of mineral pigments and color saturation. Applied optics. 2011;50(16):2464–73. doi:10.1364/AO.50.002464

Accepted Manuscript

ACCEPTED MANUSCRIPT

56. Brus LE. Electron–electron and electron-hole interactions in small semiconductor crystallites: The size dependence of the lowest excited electronic state. J Chem Phys. 1984; 80(9):4403-9.

57. Bohren CF, Huffman DR. Absorption and scattering of light by small particles: John Wiley & Sons; 2008.

ACCEPTED MANUSCRIPT